ISTANBUL TECHNICAL UNIVERSITY ★ INFORMATICS INSTITUTE

PADDY-RICE LEAF AREA INDEX (LAI) ESTIMATION USING RADAR AND OPTICAL IMAGERY

M.Sc. THESIS

Elnaz Najatishendi

Communication System Department

Satellite Communication and Remote Sensing Program

Thesis Advisor: Assoc. Prof. Dr. Esra Erten

May 2017

PADDY-RICE LEAF AREA INDEX (LAI) ESTIMATION USING RADAR AND OPTICAL IMAGERY

M.Sc. THESIS

Elnaz Najatishendi
(705121003)

Communication System Department

Satellite Communication and Remote Sensing Program

Thesis Advisor: Assoc. Prof. Dr. Esra Erten

May 2017

RADAR VE OPTİK GÖRÜNTÜLER KULLANARAK ÇELTİK BİTKİSİ YAPRAK ALAN İNDEKS KESTİRİMİ

YÜKSEK LİSANS TEZİ

Elnaz Najatishendi
(705121003)

İletişim Sistemleri Anabilim Dalı

Uydu Haberleşmesi ve Uzaktan Algılama Programı

Tez Danışmanı: Assoc. Prof. Dr. Esra Erten

Mayıs 2017

Elnaz Najatishendi, a M.Sc. student of ITU Informatics Institute Engineering and Technology 705121003 successfully defended the thesis entitled "PADDY-RICE LEAF AREA INDEX (LAI) ESTIMATION USING RADAR AND OPTICAL IMAGERY", which he/she prepared after fulfilling the requirements specified in the associated legislations, before the jury whose signatures are below.

Thesis Advisor :   **Assoc. Prof. Dr. Esra Erten**   ....
Istanbul Technical University

Jury Members :   **Assoc. Prof. Dr. Füsun Balık Şanlı**   ....
Yıldız Technical University

Asst. Prof. Dr. Gülşen Taşkın Kaya   ....
Istanbul Technical University

Date of Submission :   **5 May 2017**
Date of Defense :   **5 June 2017**

To my father, mother, spouse and child,

FOREWORD

This master thesis, titled "PADDY-RICE LEAF AREA INDEX (LAI) ESTIMATION USING RADAR AND OPTICAL IMAGERY", was prepared as a completion to the master degree in Satilate Comunication and Remote Sensing Program at the Informatic Institute of Istanbul Technical University.

As it is well known, Rice is one of the most important crops as it is the staple food for more than 3.5 billion people worldwide. The focus area of this study was the estimation of Leaf Area Index (LAI) of paddy rice crop by making use of satellite images as this variable can be used as indicator of the growth and productivity of the crop.

June 2017   Elnaz Najatishendi
                                                                                (Engineer)

x

TABLE OF CONTENTS

ABBREVIATIONS

EM   **:** Electromagnetic
GFT   **:** Gap Fraction Threshold
GA   **:** Genetic Algorithm
GMI   **:** Gitelson and Merzlyak Index
GNDVI   **:** Green Normalized Difference Vegetation Index
HH   **:** Horizontal-Horizontal
IWS   **:** Interferometric Wide Swath
LAI   **:** Leaf Area Index
MLA   **:** Mean Leaf Angle
NDWI   **:** Modified Normalized Difference Water Index
NIR   **:** Near Infrared
NDVI   **:** Normalized Difference Vegetation Index
PAR   **:** Photosynthetically Active Radiation
SR   **:** Simple Ratio Index
SAR   **:** Synthetic Aperture Radar
TOPS   **:** Terrain Observation With Progressive Scan
TC   **:** Transmission Coefficient
VH   **:** Vertical-Horizontal
VV   **:** Vertical-Vertical
WCM   **:** Water Cloud Model
ZWSI   **:** Zygielbaum Water Stress Index

SYMBOLS

r	**:**	Correlation coefficient
σ^0	**:**	Backscatter coefficient or Sigma nought
σ^0_{veg}	**:**	Backscatter coefficients from vegetation
σ^0_{soil}	**:**	Backscatter coefficients from soil
A	**:**	Digital number of the image
α_d	**:**	Incidence angle at target position
K	**:**	Absolute calibration factor
θ_i	**:**	Incidence angle
τ^2	**:**	Yields the two-way vegetation attenuation
M_v	**:**	Volumetric soil moisture
σ^0_{BG}	**:**	Sigma nought flooded surface condition

LIST OF TABLES

LIST OF FIGURES

PADDY-RICE LEAF AREA INDEX (LAI) ESTIMATION USING RADAR AND OPTICAL IMAGERY

SUMMARY

Rice is one of the most important crops as it is the staple food for more than 3.5 billion people worldwide. As a result, a number of studies have been conducted in order to improve the production and productivity of rice. One of the focus areas of the studies is the estimation of rice variables by making use of satellite images as the variables can be used as indicators of the growth and productivity of the crop. Leaf Area Index (LAI), a dimensionless index defined as the leaf area per unit ground area, is one of the most crucial biophysical variables used for monitoring the growth and productivity of crops. However, undertaking field measurement of LAI over a large area is not feasible and, thus, the use of satellite data to rapidly and accurately compute LAI values has been considered as the most convenient way. The objective for this study was to evaluate the performance of rice LAI estimation using satellite-based radar and optical images compared with in-situ measurements. *In-situ* LAI measurements were collected with CI-110 from six paddy rice fields located in Ipsala region (Yenikarpus farm), which is one of the major rice producing areas in Turkey. Paddy rice crop has three growth stages: vegetative stage (germination to panicle initiation), reproductive stage (panicle initiation to flowering) and ripening stage (flowering to mature grain). The CI-110 based field measurement was carried out during the reproductive stage of the paddy rice crop.

The satellite images used as data sources for estimating the LAI of the rice crop in the study area were captured by two Synthetic Aperture Radar (SAR) sensors named Sentinel-1 and TerraSAR-X and an optical sensor known as Landsat-8 during the reproductive stage of paddy rice crop. Both Sentinel-1 and TerraSAR-X operate in all-weather conditions. However, Sentinel-1 operates in C-band with 5.405 GHz frequency, 0-100 MHz bandwidth and VV and VH polarization, whereas TerraSAR-X operates in X-band with center frequency of 9.65 GHz, bandwidth of 300 MHz and VV and VH polarization.

Once the SAR images were collected, all images were pre-processed to account for geometric distortions due to acquisition geometry of the imagery, and backscattering coefficients were calculated. The backscattering coefficient values were then used as inputs into the Water Cloud Model to determine LAI. The reliability of this technique of determining LAI was investigated by comparing the estimated LAI results with the values of the *in-situ* LAI measurements by taking into consideration the correlation coefficients (R) as performance evaluation criteria. With regards to the optical sensors (Landsat-8 images), the Normalized Difference Vegetation Index (NDVI), Modified Normalized Difference Water Index (NDWI), Green Normalized Difference Vegetation Index (GNDVI), Gitelson and Merzlyak Index (GMI), Simple Ratio Index (SR) and Zygielbaum Water Stress Index (ZWSI) were calculated for each pixel of the 6 paddy-rice fields. Here again, correlation coefficient was used

to investigate the presence of relationships between the *in-situ* LAI values and the above mentioned indices generated from the Landsat-8 image. The results of the study showed that, in general, the indices generated from the Landsat-8 image were found to be highly correlated to the *in-situ* LAI than the values of the backscattering coefficients determined from the Sentinel-1 and TerraSAR-X images with various polarizations. In particular, the SR index was found to be the best index ($R = 0.91$) related to the *in-situ* LAI values followed by the NDVI, NDWI and GNDVI indices. In conclusion, based on the results of this study, it could be stated that Landsat-8 images could be used as a reliable data source to acquire reliable LAI for paddy rice crop in the study area much better than SAR images. Here again, it should be noted that only the reproductive stage (not time series based analyses) of paddy rice crop was considered to meet the objective of this study.

RADAR VE OPTİK GÖRÜNTÜLER KULLANARAK ÇELTİK BİTKİSİ YAPRAK ALAN İNDEKS KESTİRİMİ

ÖZET

Pirinç, dünya çapında 3,5 milyardan fazla insanın temel gıda maddesi olan en önemli ürünlerden biri olmasının yanısıra dünyada en çok tüketilen ve ekonomik olarak da en önemli besin ürünüdür. Bu konuda yapılan bir dizi çalışmanın sonucu, gelecekte artan nüfusu beslemek için pirinç üretiminin artacağını göstermektedir. Konunun bu derece önemine rağmen son gözlemler bazı alanlarda sulamadan dolayı toprak bozulmasının ve çevre kirliliğinin meydana geldiğini ve bundan dolayı pirinç verimliliğinin azaldığını hatta durduğun göstermiştir.

Bu zorlukları gidermek ve gıda güvenliğini sağlamak için pirinç üretiminde ekin değişkenlerini belirlemek, analiz etmek ve elde edilen pirinci izlemek büyük önem taşımaktadır. Bu doğrultuda, pirinç üretimini ve verimliliğini artırmak amacı ile bir takım çalışmalar yapılmıştır. Bu çalışmaların odak noktası, pirinç değişkenlerini tahmin etmek için uydu görüntülerini ürünün büyüme ve üretkenlik göstergesi olarak kullanmaktır.

Yaprak alan endeksi (LAI), birim zemin alanı başına düşen yaprak alanı olarak tanımlanan boyutsuz bir indekstir ve bitkilerin büyümesini ve verimliliğini izlemek için kullanılan en önemli biyofiziksel değişkenlerden biridir. Saha çalışmaları ile LAI'nın belirlenmesi büyük tarım alanı için zaman alıcı ve yorucudur. Uzaktan algılama ile elde edilen coğrafik verilerin kullanılması gibi dolaylı yöntemler ise güvenilirlik ve kullanım kolaylığının yanında güncel ve tutarlı bir uzamsal ve zamansal kapsama ve çözünürlüğe sunma yeteneğine sahip oldukları için yaygınlık kazanmıştır. Ayrıca LAI'nın geniş bir alan üzerinde ölçümünün yapılması mümkün değildir. Bu nedenle LAI değerlerini hesaplamak için hızlı ve doğru bir şekilde elde edilen uydu verilerini kullanmak en uygun yöntem olarak düşünülmüştür. Bu çalışmanın amacı, pirinç üretiminde LAI tahmininde ve değerlendirmesinde kullanılan uydu tabanlı radar ve optik görüntülerinin performansını yerinde (saha) ölçüm değerleri ile karşılaştırmalı olarak göstermektir.

Çalışma sahası olarak Türkiye'nin önde gelen pirinç üretim alanlarından biri olan İpsala bölgesi seçilmiştir. Bu bölge Meriç nehri boyunca 16×6 kilometre karelik bir alanı kaplamaktadır ve tarımsal arazi sulaması bu nehir ve yan kolları ile yapılmaktadır.

Çeltik ekiminin büyümesi üç aşamadan oluşmaktadır: Bitkisel, üreme ve olgunlaşma aşaması. Yerinde (saha) LAI ölçümleri, CI-110 ölçüm cihazı ile üretimin üreme aşamasında (28 Ağustos 2015 tarihinde) ve bu bölgede bulunan 6 çeltik tarlasında yapılmıştır. CI-110 ölçüm cihazı kullanılarak su ile kaplı yüzeyden 30 santimetre yükseklikte dijital yarıküresel görüntüler alınmıştır. Cihaz, 7×7 metrekare civarındaki herbir alanın kenarlarından yaklaşık 5 metre içeriden 10 dakikalık herbir periyot için 5 saniyelik veri toplamaya ayarlanmıştır. Bu cihaz aynı zamanda çalışma bölgesindeki pirinç mahsulünün "gap fraction threshold (GFT)", "photosynthetically

active radiation (PAR)", "transmission coefficient (TC)" ve "sunflecks ve mean leaf area index (MLA)" parametrelerini aynı anda ölçmek için kullanılmıştır.

CI-110, Global Navigation Satellite System (GNSS) ve aydınlanma sensörüne gelen verileri analiz ederek, ölçüm yapılan noktadaki güneş konumunu belirlemekte ve yarım küre lens ile fotoğraf alımı gerçekleştirmektedir. Daha sonra elde edilen bu fotoğraflar, kontrollü olarak sınıflara (açıklık, yeşil alan vb.) ayrılmaktadır. Sınıflandırmanın ardından otsu eşik değer metodu ile ikilik sisteme dönüştürülerek elde edilen binary görüntü üzerinde bitki sinifina giren piksellerin alani hesaplanmaktadir. Yapilan bu basit görüntü işleme algoritmaları ile, referans veri olarak alinan yarim küre foroğraflamadan yaprak alan indeksi elde edilmiştir.

Çalışma alanındaki pirinç mahsulünün LAI'sini elde etmek için uzaktan algılama görüntüleri kullanılmıştır. Uzaktan algılama sisteminde aktif (RADAR) ve pasif (optik) olmak üzere iki farklı tipte sensörler kullanılmıştır.

Aktif sensörler (radar) kendi elektromagnetik dalgasını gönderen ve bu dalganın cisme çarparak geri dönen radyasyonunu tespit eden sensörlerdir. Nesnelerin iki veya üç boyutlu görüntülerini oluşturmak için en çok tercih edilen görüntüleme radarı olduğundan ve uydu platformuna yerleştirilen büyük bir radar anteninin ileri hareketinin avantajlarından yararlanarak geleneksel ışın tarama radarlarından daha ince uzaysal çözünürlükte görüntüler elde etme özelliğine sahip olduğu için "synthetic aperture radar (SAR)" görüntüleri bu tezde kullanılmıştır.

Çalışma alanındaki pirinç mahsulünün LAI'sini elde etmek için kullanılan SAR sensörleri olan Sentinel-1 (VV ve VH polarizasyona sahip olan C-bandında) ve TerraSAR-X (VV ile HH polarizasyon olan X bandında) tüm hava şartlarında görüntü sağlama özelliği ile tarım çalışmaları için oldukça uygundur.

Sentinel-1 görüntüsü 27 Ağustos 2015'te (üreme aşamasında) «ESA» web sayfasından ve TerraSAR-X görüntüsü 4 Eylül 2015'te «Airbus Defense and Space» web sayfasından indirilmiştir. Çalışma alanı için SAR görüntüleri elde edildikten sonra bu görüntüler, her pikselin geri saçılma katsayılarını (backscattering coefficients) belirlemek için "Snap" yazılımında girdi olarak kullanılmıştır. Bu geri saçılma katsayı değerleri daha sonra LAI'yi belirlemek için su bulutu modelinde (Water Cloud Model) girdi olarak kullanılmıştır. Belirli bir dalga boyu için bir hedefin geri saçılması hedefin fiziksel boyutu, elektriksel özellikleri ve nem içeriği, daha ıslak nesnelerin parlak görünmesi ve kuru hedeflerin karanlık görünmesi gibi çeşitli parametrelere ve koşullara bağlıdır. Su bulutu modelinde bitki örtüsünün rastgele dağılmış su damlacıklarını içerdiği varsayılır ve girdi olarak geri saçılma katsayısı (dielektrik sabiti, dalga boyu, polarizasyon ve etki açısına bağlı olan bir katsayı) kullanılarak LAI değeri belirlenir. LAI'nin belirlenmesinde bu tekniğin güvenilirliği, modellenmiş LAI sonuçları ile yerinde (arazi) LAI ölçümlerinin değerleri ile karşılaştırılarak ve korelasyon katsayısı (correlation coefficient, r) dikkate alınarak araştırılmıştır.

Daha önce de belirtildiği gibi bu tezde X ve C bandı SAR işaretlerini LAI parametresiyle ilişkilendirmek için Water Cloud Model (WCM) kullanılmıştır. Bu amaçla WCM'de ihtiyaç duyulan vejetasyon parametreleri olan A, B ve C, D toprak parametreleri optimize edilmelidir. Parametrelerin optimizasyonu ve vejetasyon parametrelerinin tahmininde en uygun olan GA (genetic algorithm) bu çalışmada bir optimizasyon tekniği olarak kullanılmıştır. GA zor problemlerin hızlı, güvenilir ve doğru bir şekilde optimizasyonu için uygun bir çözümdür.

Pasif (optik) sensörler yansıtılan güneş radyasyonunu ve görünür yeryüzeyini yakın kızılötesi (NIR) ve kısa dalga kızılötesi bantlarla; yüzey tarafından yayılan radyasyonu ise termal kızılötesi bant ile algılamaktadır.

En yeni multispektral görüntüleme sistemlerinden biri olan Landsat-8 görüntüleri bu tezde kullanılmıştır. Yaklaşık 16 gün tekrarlama süresi ve 30 metre uzaysal çözünürlükte (görünür, NIR, SWIR), 100 metreden (termal) ve 15 metreden (panokromatik) olmak üzere iki görüntü algılayıcıdan oluşan bu sensörün tez çalışma alanını içeren, 11 banda sahiptir. Performans değerlendirme kriterleri olarak bu bantların yardımıyla ve ENVI programını kullanarak normalize edilmiş farklı bitki örtüsü endeksi (NDVI), modifiye normalize fark su indeksi (NDWI), çeltik-çeltik parsellerinin her pikseli için normal normalizasyon fark vejetasyon indeksi (GNDVI), Gitelson ve Merzlyak indeksi (GMI), basit oran indeksi (SR) ve Zygielbaum su stres indeksi (ZWSI) hesaplanmıştır.

Çeltik pirinç mahsulünün LAI değerleri ile ZWSI, SR, GMI ve GNDVI endeksleri arasında bir ilişki kurmak için bu endekslerin değerleri 28 Ağustos 2015 tarihinde çalışma alanının Landsat-8 uydusu ile çekilmiş olan görüntüsü kullanılmıştır. Daha sonra bu endekslerin değerleri ile yer ölçümlü LAI değerleri arasındaki ilişkiyi araştırmak için korelasyon analizi yapılmıştır. Özellikle SR indeksi, ölçülmüş ilgili LAI değerleriyle en ilişkili endeks ($R = 0.91$) olarak bulunmuştur; bunu sırasıyla NDVI, NDWI ve GNDVI endeksleri izlemektedir.

Sonuç olarak Landsat-8 görüntüsünden elde edilen indeks değerlerinin Sentinel-l ve TerraSAR-X SAR görüntülerinin çeşitli polarizasyonlarından elde edilen geri saçılma katsayı değerleriyle elde edilen indeks değerlerine kıyasla üreme döneminde elde edilen yer ölçüm LAI değerleri ile daha yüksek oranda korelasyona sahip olduğu görülmüştür. Ayrıca bu çalışma alanının çeltik ürününün LAI değerinin tahmin edilmesinde optik algılayıcının (Landsat-8) görüntülerinin SAR (Sentinel-1 ve TerraSAR-X) görüntülerinden daha hızlı ve yüksek doğruluklu bir veri kaynağı olduğu söylenebilir. Son olarak belirtmek gerekir ki, çeltik pirinç mahsulünün sadece üreme aşamasının (zaman serilerine dayalı olmayan analizler) bu çalışmanın amacına uygun olduğu düşünülmektedir.

Kısaca çeltik bitkisinin üreme döneminde gerçekleştirilen analizlerde, Landsat-8 den elde edilen SR endeksi, TerraSAR-X ve Sentinel-1 den elde edilen SAR geri saçılım değerlerine göre saha çalışmalarından elde edilen LAI ölçümleri ile daha uyumlu olduğu görülmüştür.

1. INTRODUCTION

Rice is the most widely consumed and economically important food crop in the world [1]. A number of studies show that the production of rice will increase in the future to feed the world's increasing population. Despite its importance, however, recent observations indicate that the productivity of rice has become stagnant or even declined because of land degradation and environmental pollution in some irrigated areas [2]. In order to address these challenges and optimize food security, rice monitoring, which is achieved through the determination and analysis of rice crop variables, is very important [3]. Paddy rice crop has three growth stages: vegetative stage (germination to panicle initiation), reproductive stage (panicle initiation to flowering) and ripening stage (flowering to mature grain).

Leaf Area Index (LAI), which is defined as the total one-sided leaf area per unit ground area is one of the most important biophysical crop parameters that characterize the canopy of the crop [4]. The calculation of LAI using direct method is time-consuming and destructive. As opposed to this, indirect methods such as using remotely sensed geospatial data of rice fields with updated spatial and temporal resolution has gained popularity because of their reliability and ease of operation in addition to their ability to provide timely and consistent spatial and temporal coverage [5].

This research project investigated the potentials of Synthetic Aperture Radar (SAR) images particularly obtained from Sentinel-1 and TerraSAR-X and optical images obtained from Landsat-8 as reliable and quick data sources for generating the LAI of a paddy rice crop.

The objectives of this study were:

• To investigate the relationship between the *in-situ* LAI and measured field parameters such as Photosynthetically Active Radiation (PAR), Gap Fraction Threshold (GFT), Sunflecks, Transmission Coefficient (TC) and Mean Leaf Angle (MLA).

- To investigate the relationship between the *in-situ* LAI and radar observations including backscattering coefficients in different frequency, polarization and resolution,

- To investigate the correlation analysis between vegetation indices such as, the Normalized Difference Vegetation Index (NDVI), Simple Ratio Index (SR), Green Normalized Difference Vegetation Index (GNDVI), Modified Normalized Difference Water Index (NDWI), Gitelson and Merzlyak Index (GMI) and Zygielbaum Water Stress Index (ZWSI) from Landsat-8 satellite images and *in-situ* LAI measurements.

- To investigate the reliability within different sensors in terms of LAI estimation,

1.1 Literature Review

LAI, defined as the ratio of the total area of all leaves on a plant to ground surface area, is one of the most important crop parameters used for monitoring crop biophysical parameters, yield estimation and gas exchange processes in plants [6–9]. Due to this importance, a significant number of studies have been undertaken and a considerable amount of knowledge has been accumulated in the literature as to how to obtain rapid, reliable and accurate estimation of LAI. The methods can be divided into two categories: direct and indirect methods.

The direct methods involve actual field measurements with destructive or non-destructive techniques. They involve the collection and measurement of leaf area, using either a leaf area meter or a specific relationship of dimension to area via a shape coefficient [10]. According to [11], planimetric and gravimetric methods are identified as the two direct methods of leaf area determination. The planimetric method is based on the correlation between the individual leaf area and the number of area units covered by that leaf in a horizontal plane whereas the gravimetric method is based on the correlation between dry weight of leaves and leaf area using predetermined leaf mass per area. The direct method is, therefore, complex, time-consuming, laborious and expensive as it involves intensive sampling and require the use of special measuring instruments. Due to the difficulties and the limitations of the direct methods, they are mostly used as reference data for indirect methods which are easier and faster to apply.

The indirect methods are cost effective and have the advantage of obtaining a large-scale information in a very short period of time and, thus, the variable being studied is better assessed. Among the indirect methods of LAI estimation, the hemispherical canopy photography (also known as fisheye lens photography), is being applied successfully in commercial plantations. The hemispherical canopy photography is based on estimated position, size, density and distribution of canopy gaps, which characterize the canopy geometry, through which the solar radiation intercepted is measured [12]. From the research point of view, the current trend of photography based indirect measurements is going towards smartphone applications [12].

Other indirect measurements involve the use of space-based technologies. These technologies obviate the need for land-based surveys and provide a possible effective method to address the problems associated with direct methods of LAI determination. Hence, the use of spaceborne remote sensing images for analysis of agricultural fields has rapidly increased due to its inherent nature in supplying easy, fast and accurate solutions [13, 14]. Satellite-based indirect methods can roughly be grouped under two categories: radar and optical observations. LAI monitoring with optical sensors started with MODIS [15]. After having successful results, the studies have continued with high-resolution satellite data such as Landsat, Spot, and Sentinel-2. From a methodological point of view, LAI can be estimated from spectral (vegetation) indices computed by using these satellite data instead of dealing with *1 to n* ill-posed advanced radiative transfer model [12, 16]. This can be achieved as the interaction between the wave and the target causes different reflectance due to the pigments and plant components, which allows to the creation of a large number of vegetation indices with different sensibilities [17]. Although these indices are not well suited for direct LAI estimation, their ease of computation and tackling the problem of leaf inclination angle makes them popular for space-based crop monitoring.

Spaceborne radar systems are also of interest for agricultural studies. They are particularly important for irrigated farming with their all weather, day and night imaging capability [18]. The latest generation of radar imaging satellites features high temporal and spatial resolution as well as enhanced capabilities of polarimetric acquisition. Radar backscatter measurements depend on physical and geometrical

properties of the target. Previous studies showed that there is a strong relationship between radar backscattering and biophysical properties of crops such as LAI, biomass, and crop height [19]. Radar backscattering based LAI measurements can be divided into two categories: modeling the radiative transfer of SAR beam (inverse problems) and statistical analysis. Modeling radiative transfer involves inverse problem of *1 to n* relationship between radar backscattering and morphological and physical properties of the crop, requiring powerful nonlinear inversion methods [20]. Instead, statistical approaches relate the radar backscattering measurements with in-situ based LAI measurements and generalize the results.

There are two approaches in the literature that are used to relate the SAR signatures to the LAI parameter: empirical and semi empirical approaches. An example of the later approach is the use of a model termed as Water Cloud Model (WCM). WCM, a model where the canopy cloud is assumed to consists of identical, randomly distributed water droplets within the canopy, is used to determine LAI by using the backscatter coefficient (a coefficient that depends on the dielectric constant, wavelength, polarization, and incidence angle) as input.

In this study, the LAI estimation results determined by using Landsat, TerraSAR-X and Sentinel-1 images with the aim of analyzing the performance of free satellite imagery in terms of crop monitoring are presented. Paddy rice fields, which had reached late reproductive stage are used for showing the feasibility and the operational capability of the sensors with simplified methods [21, 22].

1.2 Structure of the thesis

This thesis is structured as follows. **Chapter 2** gives a general introduction to the fundamental theories about the SAR and optical remote sensing. In **Chapter 3**, material and methods used to meet the objectives of the thesis are presented. More specifically, the data collection and analysis for the CI-110 based *in-situ* LAI measurements, the Landsat-8 based LAI determination, and the Sentinel-1 and TerraSAR-X based Radar LAI computations are discussed. Moreover, a brief description of Genetic Algorithm (GA) is given. In **Chapter 4**, the results of the methods used to determine LAI and their comparisons are presented and discussed.

The final chapter, **Chapter 5**, is given to contain a brief summary of the study, concluding remarks and recommendations for future work.

2. THEORY

Remote sensing is the process of gathering information about an object without any direct contact with the object. Despite the presence of various types of systems, remote sensing based data acquired by space-borne platforms are of paramount importance for systems aiming to provide large-scale mapping [23]. Remote sensing uses a part or several parts of the Electromagnetic (EM) spectrum, which is a continuum of all EM waves energy reflected or emitted by the earth's surface arranged according to frequency and wavelength. There are two primary types of remote sensing systems: passive (optical) and active. Active sensors send their own EM wave and then detect scattering returning from an object. As opposed to these, passive sensors, also known as optical sensors, detect emitted and/or reflected EM radiation from an object, but the source of the EM wave is a natural source such as the Sun.

Active sensors are known to be operated day and night, less weather dependent and have controlled illuminating signal that is not affected by the atmosphere. Because of these advantages, active sensors have been applied in various field of studies such as oceanography, hydrology, geology, glaciology, agriculture, and forestry. Thus, they are much more advantageous than passive sensors and have the potential to provide accurate information [24].

Radar, an abbreviation taken from Radio Detection and Ranging, is one of the most popular active imaging sensors. In particular, SAR is the most widely used radar type of active imaging sensor. The following sections are given to describe the fundamentals of SAR and optical imaging sensors.

2.1 SAR fundamentals

The most versatile radar instrument that is used to create either two or three dimensional images of objects is the SAR. SAR takes advantages of the forward motion of a large radar antenna placed on the platform of the satellite to provide images with finer spatial resolution than is possible with conventional beam-scanning radars.

7

The SAR satellites function at selected frequencies. However, the predominantly used spaceborne wavelengths are the L-band, C-band, and X-band. Some of the sensors that use these bands are RadarSAT-2 (C-band), Sentinel-1 (C-band), ALOS-2 (L-band), Cosmo-Skymed (X-band) and TerraSAR-X (X-band) [25]. In this study, Sentinel-1 and TerraSAR-X images are used.

Backscatter of a target at a particular wavelength depends on a variety of conditions such as the physical size of the target, the target's electrical properties and the moisture content, the wavelength and polarization of the Radar pulses and observation angles also affect backscatter. Figure 2.1 depicts the backscatter from various targets.

Mountains   Forest   Flat Surface   Crop land   Rough Surface   City
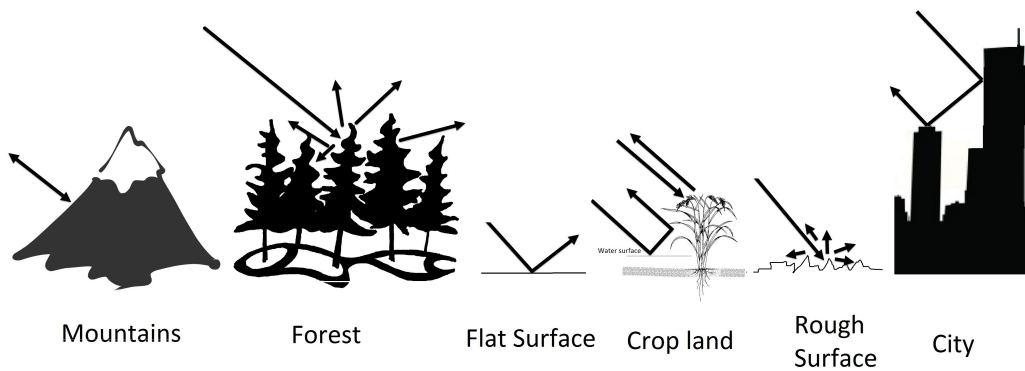
Figure 2.1 : Backscatter from various surfaces types

The wavelength and polarization of the Radar pulses and observation angles also affect backscatter. The relationship between the image intensity and the backscattering coefficient $\left(\sigma^0\right)$ is given by:

$$\sigma^0 = \frac{A^2}{K} sin(\alpha_d) \tag{2.1}$$

,where σ^0 is the radar backscattering coefficient of distributed target to be measured, A is the digital number of the image, α_d is incidence angle at target position, K is absolute calibration factor.

Thus, the backscattering coefficient can be used to determine the LAI of vegetation with the help of empirical or semi-empirical models. WCM is a semi-empirical model that is developed to find a linear relationship between LAI and backscattering coefficients determined from SAR images of polarizations. It should be noted here that, the differences in the characteristics of the Sentinel-1 and TerraSAR-X images

are expected to result in differences in the values of backscattering coefficients. This in turn results in different estimates of LAI values.

As a semi-empirical model, WCM defines the backscatter coefficient or sigma nought (σ^0) as a linear combination of backscatter coefficients from vegetation (σ_{veg}^0) and from soil (σ_{soil}^0). WCM was first developed by [22] and was then applied to the assessment of LAI by [26]. In WCM, it is assumed that the canopy cloud consists of identical water droplets randomly distributed within the canopy and the backscatter coefficient, which depends on the dielectric constant, wavelength, polarization, and incidence angle θ_i, is written as [12, 21, 27]:

$$\sigma_{pq}^0 = \sigma_{veg}^0 + \tau^2 \sigma_{soil}^0 \qquad p, q = H, V \tag{2.2}$$

$$\sigma_{veg}^0 = AV_1 \cos \theta_i (1 - \tau^2) \tag{2.3}$$

$$\sigma_{soil}^0 = C + DM_v \tag{2.4}$$

$$\tau^2 = \exp\left(-2BV_2 \sec \theta_i\right) \tag{2.5}$$

where τ^2 yields the two-way vegetation attenuation, M_v is the volumetric soil moisture, V_1, V_2 are the descriptors for canopy and σ_{veg}^0 and σ_{soil}^0 are the backscatter coefficient for vegetation and soil of respectively.

In the WCM, the vegetation parameters A, B and the soil parameters C, D are empirically obtained. Due to the flooded condition of the fields during the rice growing season, the simplification of the backscattering model is proceeded by replacing σ_{soil}^0 by constant σ_{BG}^0 and by assuming $V_1 = V_2 = V$. As implemented by [26] and [28], the backscattering coefficient for the paddy rice can be expressed (in dB) as in the following.

$$\sigma^0 = 10 \log \left\{ AV \cos \theta_i \left(1 - \exp\left[-2BV \cos \theta_i\right]\right) + \exp\left[-2BV \cos \theta\right] \sigma_{BG}^0 \right\} \tag{2.6}$$

Using LAI as a canopy descriptor (V1 = V2 = V = LAI) in WCM yields the optimization problem of finding A, B, and σ_{BG}^0 . In this work, Genetic Algorithm (GA) optimization approach was used to estimate the vegetation parameters as it is best suited for optimization of parameters [29].

2.2 Optical Remote Sensing Fundamentals

Passive sensors, detect solar radiation reflected by the earth's surface in the visible, near infrared (NIR) and short-wave infrared bands and the radiation emitted by the surface in the thermal infrared band, recorded as brightness temperature by the sensor to form images of the earth's surface [30]. By taking into consideration the number of spectral bands used in the imaging process, optical (passive) remote sensing techniques are classified as Panchromatic, Multispectral, Superspectral and Hyperspectral imaging systems [31]. The multispectral imaging system is equipped with a multichannel detector with a few spectral bands, where each channel is sensitive to radiation within a narrow band of wavelength resulting in a multilayer image that contains both the brightness and spectral information of the observed objects. As a result, images captured with multispectral imaging systems are used in a number of applications [32].

LANDSAT MSS, LANDSAT TM, SOPT HRV-XS and IKNOS MS are a few examples of multispectral space-borne imaging systems. One of the most recent multispectral imaging system is Landsat-8 with 16 days of revisit time and at a spatial resolution of 30 meters (visible, NIR, SWIR), 100 meters (thermal) and 15 meters (panchromatic) `https://landsat.usgs.gov/what-are-band-designations-landsat-satellites`. Detail characteristics of the spectral bands of Landsat-8 imaging system are presented in Table 2.1.

Table 2.1 : Landsat-8 Bands

Bands	Wavelength (micrometers)	Resolution (meters)
Band 1 - Coastal aerosol	0.43 - 0.45	30
Band 2 - Blue	0.45 - 0.51	30
Band 3 - Green	0.53 - 0.59	30
Band 4 - Red	0.64 - 0.67	30
Band 5 - Near Infrared (NIR)	0.85 - 0.88	30
Band 6 - SWIR 1	1.57 - 1.65	30
Band 7 - SWIR 2	2.11 - 2.29	30
Band 8 - Panchromatic	0.50 - 0.68	15
Band 9 - Cirrus	1.36 - 1.38	30
Band 10 - Thermal Infrared (TIRS) 1	10.60 - 11.19	$100 \times (30)$
Band 11 - Thermal Infrared (TIRS) 2	11.50 - 12.51	$100 \times (30)$

The mathematical combinations of surface reflectance at two or more of the wavelengths (depicted in Table 2.1) result in Spectral indices. Thus, based on the

considered reflection and absorption characteristics at different wavelengths, various indices could be developed so that targets can be discriminated in the captured Landsat images according to their spectral reflectance signatures. In the literature, spectral indices such as Vegetation, Burned areas, Man-made (built-up) features, Water, and Geologic features are available. Among these, however, spectral vegetation indices are the most popular ones. This is because these indices are simple mathematical expressions that are widely used to determine values of vegetation parameters such as plant biomass and structure (leaf size, stem density, LAI, etc.). In addition vegetation indices can be used for crop monitoring and measuring live and green vegetation amount from remotely sensed images in a short period of time with less cost.

Spectral vegetation indices are mathematical combinations of different spectral bands mostly in the visible and near-infrared regions of the EM spectrum [33]. These indices reduce the multiple-waveband data at every pixel of an image into a single numerical value (index) [34]. The values of these indices can be taken as measures of vegetation activity and as means of highlighting changes in vegetation condition. As a result, many studies have been carried out establish relationships between LAI and spectral vegetation indices determined from images captured with optical remote sensing systems [35]. The most widely used spectral vegetation indices for this purpose are: NDVI, SR, GNDVI, NDWI, GMI and ZWSI [20]. The NDVI is expresses as [36]:

$$NDVI = \frac{\rho_{NIR} - \rho_{Red}}{\rho_{NIR} + \rho_{Red}} \tag{2.7}$$

,where ρ_{NIR} and ρ_{Red} refer to the NIR and red reflectance in each band, respectively. This index is the most widely used standardized indicator of the relative biomass of plant as can be used to monitor drought, agricultural production, predict hazardous fire zones and map desertification [37]. Its values range between –1 to 1, where values close to unity depict highly vegetated targets, while values close to zero represent non-vegetated targets.

 [38] defined SR as ratio of the values of the NIR reflectance to the red reflectance as depicted in the following equation:

$$SR = \frac{\rho_{NIR}}{\rho_{Red}} \tag{2.8}$$

Non-vegetated targets such as bare soil have SR values of unity or close to unity, and this is achieved when the values of the NIR and the red reflectance are equal or almost

the same values. SR is not normalized and its values increase as the amount of green vegetation in a pixel increases.

GNDVI is defined as [39]:

$$GNDVI = \frac{\rho_{NIR} - \rho_{Green}}{\rho_{NIR} + \rho_{Green}} \qquad (2.9)$$

,where stands for the digital number of the Green channel of a pixel. GNDVI and NDVI are similar except the fact that GNDVI is based on the green spectrum instead of the red spectrum. However, GNDVI is known to be more sensitive to chlorophyll concentration than NDVI.

The NDWI is expressed as [6]:

$$NDWI = \frac{\rho_{NIR} - \rho_{SWIR1}}{\rho_{NIR} + \rho_{SWIR1}} \qquad (2.10)$$

[40] defined the GMI index as:

$$GMI = \frac{\rho_{SWIR12}}{\rho_{Green}} \qquad (2.11)$$

ZWSI is defined by [41] as:

$$ZWSI = \frac{\rho_{SWIR11}}{\rho_{Green}} \qquad (2.12)$$

3. MATERIALS AND METHODS

This section provides the dataset behind the LAI estimation study in detail along with coincide information about their processing methodology.

3.1 Description of the study area

The study area, Ipsala, is located in north western part of Turkey at (N $37^o7'53''$ and E $6^o19'32''$). It is a rice-agricultural field with an area of 16×6 km and found along the Maritza River, which forms, with its tributaries, the drainage system for the irrigation of the paddy rice fields. Ipsala site is one of the largest rice-producing areas in Turkey. The most dominant rice species in this area is *Oryza sativa L.*; specifically the two long-grain types: Baldo and Rocca are common in the area. In this region, rice crops are planted by broadcasting. The planting techniques used by the farmers vary from the use of airplane to manual labor, but in all of the techniques, seeds spread randomly. This agronomic practice characterizes the heterogeneity within and among the fields. Accordingly, the sowing date can vary from the end of April to late May and the harvest takes place in the late September to mid October. The rice-agricultural fields, shown in Figure 3.1, are cultivated annually. Since 2013, the Directorate of Trakya Agricultural Research Institute has collected ground measurements in the area to develop an operational satellite based monitoring scheme [26, 28, 42–45].

3.1.1 *In-situ* LAI measurements: CI-110

Ground measurements of LAI for paddy-rice were performed with the CI-110 Plant Canopy Imager. This device was also used to simultaneously measure the Gap Fraction Threshold (GFT), Photosynthetically Active Radiation (PAR), Transmission Coefficient (TC), Sunflecks, and MLA parameters of the rice crop in the study area. The measurements of the *in-situ* LAI and the above listed other crop biophysical parameters were collected from 6 paddy rice plots (Figure 3.1) on the August 28, 2015 during the late reproductive stage of paddy rice. Digital hemispherical images using
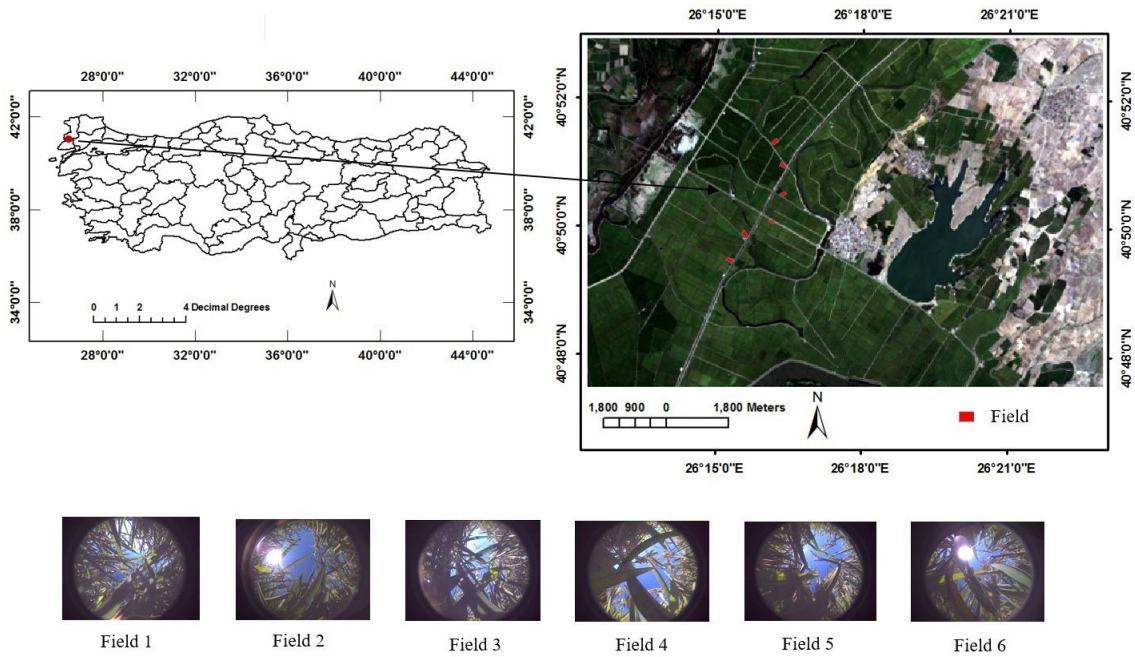
Figure 3.1 : Location of the study area (top left), Lansat-8 image acquired on August 28, 2015 over the study area (top right, red color indicating the locations of the six test fields analyzed in this study) and hemispherical photographs depicting the nature of paddy fields were taken with a canopy imager (CI-110) (bottom).

CI-110 were acquired at 30 centimeters from the surface covered by water. In each field, the CI-110 was programmed to collect data every 5s in 10 minutes at the four corners of the six roughly 7×7 meter fields, approximately 5 meter from the edge of the fields. The images depicted in Figure 3.1 show hemispherical images of the six paddy rice plots acquired using CI-110 (That is directly captured by CI-110 plant canopy imager). These images were processed using the CI-110 software to obtain LAI and PAR.

CI-110 analyzes inputs obtained from Global Navigation Satellite System (GNSS) and optic sensors. CI-110 uses the above mentioned inputs to determine the location of the sun in relation to the location target and it captures images with its hemispherical lens. Then, the captured image is manipulated with a software to classify green area, openness and others in a controlled manner. After achieving the controlled classification, the image is converted into a binary system using Otsu threshold value method and calculates the areas of the pixels that fall within crop class. These steps are carried out to determine the Leaf Area Index (Figure 3.2).
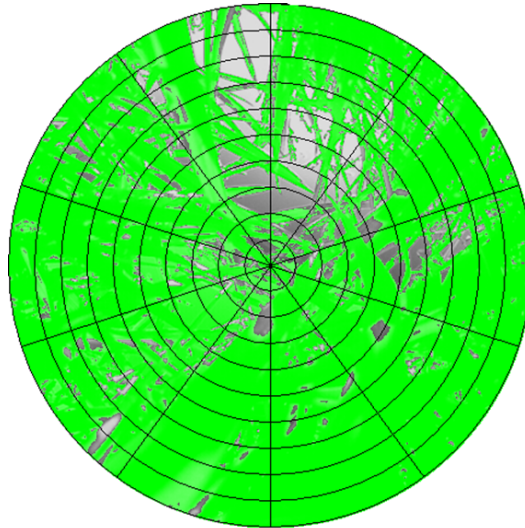
14

Figure 3.2 : Classification of LAI

3.2 Optical LAI Measurements: Landsat-8

In this study, for optical satellite imagery based LAI measurements, Landsat-8 image is used due to its relatively wide spectral range and the spatial resolution. Additionally, Landsat-8 images can be obtained freely from the United States Geological Survey (USGS: `http://landsat.usgs.gov/`) data archive system and, thus, they can be used for long term vegetation monitoring and parameter determination. In this particular study, Landsat-8 OLI data acquired on 28 August 2015 with 30 m pixel resolution were downloaded from the website of the USGS `http://landsat.usgs.gov/`. The Landsat-8 with 181 path and 032 row for Scene "LC81810322015240LGN00" covers the entire rice field. Surface reflectance of the scene for each channel (blue (B), green (G), red (R), NIR, and the two short wave infrared (SWIR1, SWIR2) were calculated by using FLAASH embedded in the ENVI software and were used to determine spectral vegetation indices. These indices are: NDVI, NDWI, GNDVI, GMI, SR and ZWSI [20], and they were determined for each field of the six paddy rice plots using the Eqs. (2.7)-(2.14).

3.3 Radar LAI Measurements: Sentinel-1, TerraSAR-X

Sentinel-1 is a long-term mission of a polar orbiting satellite launched to provide continuous all-weather day/night imagery at C-band for observation, mapping and monitoring purposes [46]. Sentinel-1 is the first satellite built with interferometric wide swath (IWS) mode exploiting the terrain observation with progressive scan (TOPS)

technique and has been designed to achieve medium-to-high-resolution imaging capabilities [47] driven by the need for continuity of data provision with improved revisit, coverage, timeliness and reliability of service [48]. The Wave Mode of Sentinel-1 has selectable single polarization (VV or HH) and for all other modes, Sentinel-1 has selectable dual polarization (VV+VH or HH+HV).

For this study, the Sentinel-1 image acquired on 27 August, 2015 was downloaded from the website of ESA `https://scihub.copernicus.eu/dhus/`. The Sentinel-1 image was processed using the Sentinel-1 Toolbox. After performing radiometric calibration, terrain correction (With SRTM) and speckle filtering with a 7×7 window, the intensity of the VV and VH polarized images were transformed to backscattering coefficients σ^0 using Eq. 2.1 with the help of SNAP software.

TerraSAR-X is a German national SAR-satellite system that features an advanced high-resolution X-Band SAR based on the active phased array technology. This technology allows the operation in Spotlight, Stripmap and Scan SAR Mode with various polarizations [49]. The radar of TerraSAR-X has single and dual polarization options. It also has an additional quad polarization option for Mission specific captures. TerraSAR-X captures in 5 modes with resolutions ranging from 1m (High Resolution Spotlight Mode) to 18.5m (Scan SAR Mode) and revisit times ranging from 2.5 days to 11 days depending on imaging mode.

It could be understood from above given characteristics of Sentinel-1 and TerraSAR-X that the images captured by these sensors are different in resolution and in frequency. Despite these differences, however, both SAR images can be used to estimate the radar backscatter of a target on the ground.

The HH and VV polarized intensity images captured on 04 september 2015 were downloaded from Airbus Defense and Space website `http://terrasar-x-archive.infoterra.de/` and they were transformed to backscattering coefficients as given in Eq.1. To reduce the speckle boxcar filter with kernel dimension of 5×20 m (*range* $\times$ *azimuth*) was used for calculating σ^0 values. Compared to Sentinel-1 imagery, the main advantage of TerraSAR-X is its high resolution imaging capability. Radar sensor parameters are given in Table 3.1.

Table 3.1 : Radar sensor parameters

Satellite Mission Parameter	TerraSAR-X X-Band	Sentinel-1 C-Band
Central frequency [GHz]	9.65	5.35
Average incidence angle [deg]	31	29
Orbit height [km]	515	693
Illuminated area x-size [m]	2.6	7.6
Illuminated area y-size [m]	1.8	5.2
Polarization	VV/HH	VV/VH
Acquisition date	2015.09.04	2015.08.27

As it is very well known, the backscattering coefficient of SAR images is a function of various variables that are affected by vegetation and soil types, topography of the land and the types of the sensor used in the radar. Because of this, the values of the backscattering coefficient need to be determined using a process-based model [28]. In addition to backscattering analysis, in this paper, in order to relate the X and C band SAR signatures to LAI parameter the WCM was used. For this purpose, the vegetation parameters A, B and the soil parameters C, D required in WCM need to be optimized.

As indicated earlier (Eq. 2.3), WCM is used to determine the backscatter coefficient of a crop (σ_{veg}^0) as a function the backscatter coefficient of the soil (σ_{soil}^0), soil parameters (C and D), canopy descriptor (V), dielectric constant, wavelength, polarization and incidence angle. In WCM, the values of σ_{soil}^0 are given in the form of soil moisture (σ_{BG}^0). However, since paddy rice fields are under water for long time, the backscattering coefficient from the surface of the soil under the crop canopy (σ_{BG}^0) can be taken as constant. In shorter, in paddy rice fields, σ_{BG}^0 and σ_{soil}^0 are assumed to be equal. In addition, the values of both canopy descriptors (V_1 and V_2) are assumed to be equal ($V_1 = V_2 = V$) and can be represented by LAI. This means that $V_1 = V_2 = V = LAI$ [29]. In this regard, WCM yields the optimized results to the values A, B and σ_{BG}^0 from LAI and GA was used as an optimization technique to estimate the vegetation parameters as it is best suited for optimization of parameters [29].

As it is very well known, GAs are the solution for optimization of hard problems quickly, reliably and accurately [50]. In other words, GA is a computerized search and optimization algorithm based on the prototype of natural selection and natural genetics [51]. Usually, a simple GA for optimization comprises six major components,

17

namely genetic representation, reproduction, cross-over, mutation, a fitness function and termination criteria [50].

Genetic representation: Initially, a population of parameters proportional to the total string length is generated using a random generator. Generally, GAs have been developed by using binary coding in which a string (or chromo-some) is represented by a string of binary bits that can encode integers or real numbers. In this study, the parameters A and B were encoded as substrings of binary digits having a specific length. These substrings are joined together to form longer strings representing a solution. The length of the substring is determined according to the desired solution accuracy and is dependent on the range and the precision requirement of the parameter [52].

Reproduction: The strings generated in the initial population are chosen for participation in the reproduction process based on their fitness values. Many selection schemes, such as deterministic sampling, stochastic sampling with or without replacement, stochastic tournament selection and fitness proportionate selection, can be used for the reproduction process [53]. In this study, fitness proportionate selection has been used, where a string is selected for the reproduction process with a probability proportional to its fitness. Thus the probability p_i of an individual member string i being selected is given by:

$$p_i = \sum_{i=1}^{n} f_i \tag{3.1}$$

,where f_i is the fitness of an individual string i and n is the population size.

The scheme is implemented with the simulation of a roulette wheel with its circumference marked for each string proportionate to the string's fitness. The roulette wheel is rotated p times, each time selecting a copy of the string chosen by the roulette wheel printer. As the circumference of the wheel is marked according to a string's fitness, the roulette wheel mechanism makes f_i/f_{mean} copies of the ith string in the reproduction. Here, f_{mean} is the average fitness of the population given as:

$$f_{mean} = \frac{1}{n} \sum_{i=1}^{n} f_i \tag{3.2}$$

18

A string with a higher fitness value represents a larger range in the cumulative probability values, and, hence, has a higher probability of being copied into the mating pool.

Mating (cross-over): The general theory behind the cross-over operation is that by exchanging important building blocks between two strings that perform well, the GA attempts to create new strings that preserve the best material from the two parent strings. Cross-over is a recombinant operator that selects two strings from the mating pool at random and cuts them into bits at a randomly chosen position. This produces two "head" segments and two "tail" segments. The tail segments are then swapped over to produce two new full-length strings. The number of strings participating in mating depends on the cross-over probability. If a cross-over probability of p_c is used, only $100 \times p_c$ percent strings in the population are used in the cross-over operation. Cross-over has a wide range of possible types, i.e. one point, multipoint, uniform, intermediate arithmetical and entered arithmetical [53]. The effect of cross-over depends upon the site at which cross-over takes place.

Mutation: Mutation is an important process that permits new genetic material to be introduced to a population. A mutation probability is specified that permits random mutations to be made to individual genes (e.g. changing 1 to 0 and vice versa for binary GAs). A mutation operator facilitates the convergence towards an optimal solution even if the initial population is far from the optimal solution. Binary genetic algorithms use a very low mutation probability ranging from 0.001 to 0.05.

Termination criteria: In the present study, the GA-based process is stopped when the fitness criterion is satisfied, or the maximum number of generations is exceeded. The values of the genetic parameters such as string length, population size, cross-over probability, reproduction, mutation and termination criteria are given in a later section.

In short, the GA calls the written code repeatedly to find the most appropriate values of the vegetation parameters A and B, which are then used to find the best relationship between X- band and C-band SAR signatures and the LAI parameter.

4. RESULTS

This section covers the LAI estimation of paddy rice fields which had reached reproductive stage on the acquisition dates.

4.1 The relationship between *in-situ* LAI and some other crop biophysical parameters

For investigation the relationship between the LAI and other crop biophysical parameters of the rice crop in this study, values of the *in-situ* LAI, GFT, PAR, Sunflecks, TC and MLA were determined using CI-110. The mean values of these parameters determined for the 6 fields are presented in Table 4.1.

Table 4.1 : Mean values of the *in-situ* LAI and other crop biophysical parameters.

Field No	Area (m^2)	LAI	PAR	Mean Leaf Angle	Transmission Coefficient	Sunflecks	Gap Fraction Threshold
1	9761	1.65	1014.61	20.83	0.218	48.96	0.765
2	14551	2.55	867.50	9.55	0.187	51.39	0.760
3	22476	2.62	848.83	16.04	0.186	43.33	0.748
4	21145	2.68	707.57	11.08	0.177	61.11	0.754
5	21784	1.71	825.40	25.45	0.253	32.22	0.769
6	20836	1.85	303.94	18.93	0.223	6.95	0.746

The correlation between the *in-situ* LAI and the other crop biophysical parameters are depicted in Figure 4.1. It can be seen from the correlation coefficient values given on the graph bar in of Figure 4.1 that there is a weak relationship between the *in-situ* LAI and the values the PAR and GFT parameters respectively as the corresponding correlation coefficient values are found to be less than 0.5. However, the TC parameter, with a correlation coefficient value of -0.905, was found to be related to the *in-situ* LAI better than these parameters, followed by MLA (with a correlation coefficient of -0.869).
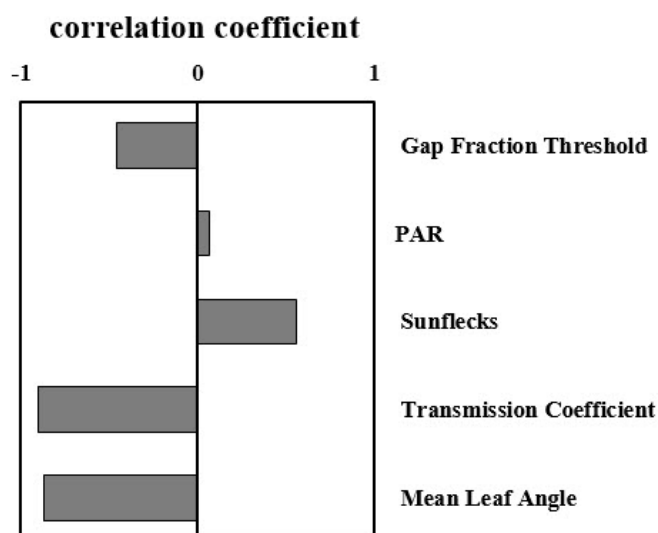
Figure 4.1 : The values of the correlation coefficients of the ground-based crop parameters and *in-situ* LAI

PAR refers to the spectral range of solar radiation (400-700 nm). It is determined as the mean light intensity over the sensors positioned along the top of the CI-110 arm. PAR can directly be measured by using the sensors. The light above the canopy has a value ranging from 1 to 2000 $\mu mol/m^2 s$.

Sunflecks refer to the occurrence an increased amount of solar radiation below the canopy within a short period of time. Wind moving leaves in the canopy or the sun's movement within a specific day are the causes of Sunflecks. The size of the Sunflecks can be used to determine the size of canopy cover and can be related to the characteristics of the canopy. The sunfleck value is a percentage of the PAR sensors exposed to a radiation level greater than the set threshold. The default sunfleck minimum PAR is set at 300 $\mu mol/m^2 s$.

The probability of a ray of light passing through the canopy without touching foliage or other plant elements is termed as Canopy gap fraction. There are several methods incorporated in the CI-110 Plant Canopy Analysis software to determine the Gap Fraction. In this study, the Otsu method was used.

An other parameter which very similar to the gap fraction is the solar beam transmission coefficients. This coefficient is defined as the fraction of the sky visible from beneath the plant canopy. This coefficient has values ranging from 0 to 1; 0 meaning no sky is visible below the plant canopy, and 1 meaning that the entire area is sky or no foliage coverage. The values of this coefficient determined for the six paddy

rice fields are presented in Table 4.1. As can be seen from this table, the transmission coefficient values are closer to zero. This is because the ground was well covered with the crop at the time of the measurement as the measurement was carried ou at the reproductive stage of the paddy rice crop.

4.2 Backscattering coefficient analysis

In order to see temporal trend of backscattering coefficient over the study area, first, a total of nine Sentinel-1 satellite images captured in June, July and August were analyzed. Radiometric calibration, terrain correction and speckle filtering were performed on these images. The corrected and calibrated images were then used to determine the values of sigma nought for each pixel in the images. The mean sigma nought values of each fields were determined for various dates under the various polarizations. These values were plotted against time and are presented in Figure 4.2 and Figure 4.3.
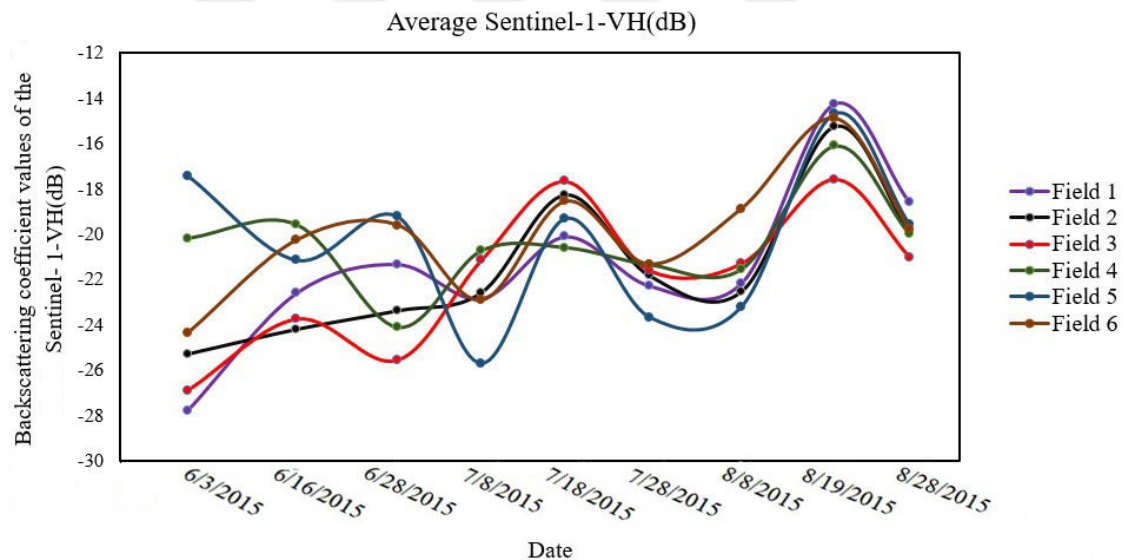
Figure 4.2 : The time series of average of sigma nought (dB) in VH polarization in 2015.

As can be seen from Figure 4.2, the mean sigma nought values of the fields determined from the SAR images with VH polarizations tend to increase and decrease with time except the fact that the sigma nought values determined from the image captured on August 28, 2015 dropped again. As opposed to this, the mean sigma nought values of the fields determined from the SAR images with VV polarizations tend to fluctuate
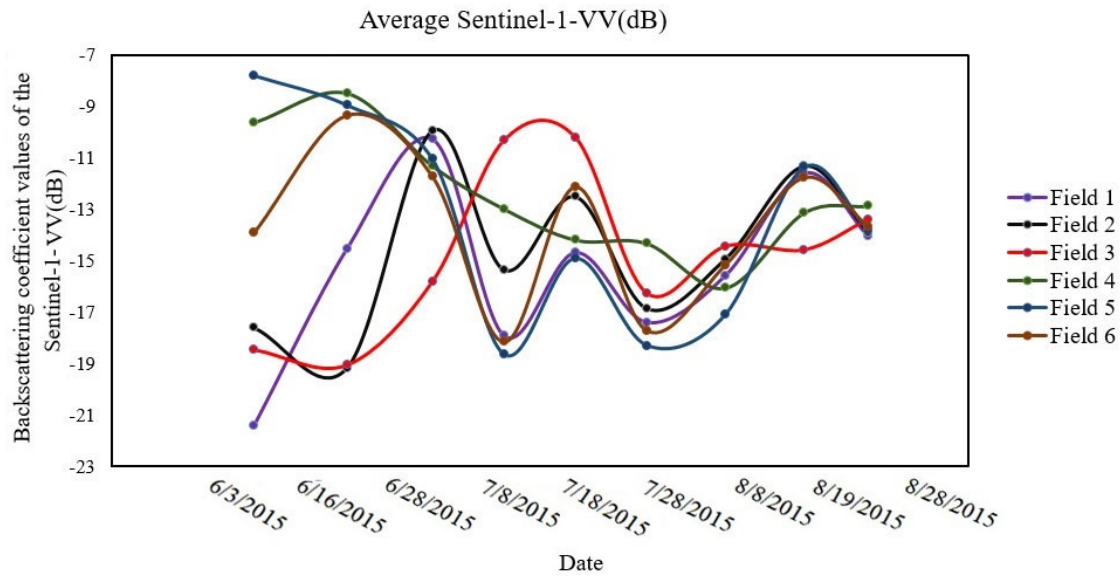
Figure 4.3 : The time series of average of sigma nought (dB) in VV polarization in 2015.

with time (Figure 4.3). However, the mean sigma nought values of the six rice fields determined from the SAR images in both VH and VV polarizations capture on June 3, 2015 are very different from one another when compared to the mean sigma nought values of the fields determined from the SAR images captured on other dates.

The time series of the variance of sigma nought(dB) values under the VH and VV polarization in 2015 are presented in Figure 4.4 and Figure 4.5 respectively. It can be clearly seen from these figures that the variance of the mean sigma nought values of the six fields under both VH and VV polarizations remained more or less below three in most of the dates. However, the variance values determined from the mean sigma nought values of the images captured on June 3, 2015 were found to be larger (for most of the fields) and very different from field to field. As the result, paddy fields are flooded during the rice-planting season (early vegetation) that has low backscatter in this season. In the general case of rough water bodies, the visible structures do not show regular wave pattern; irregular pattern is caused more frequently at the surface of paddy rice fields and this causes irregular backscattering values. Backscatter of a paddy field increases as rice grows. However, it is impossible to monitor rice fields precisely due to speckle noise of SAR data. The default of SAR data is single banded and contains speckle noise. This could be because of the considerable difference in the sigma nought values determined from the image captured on June 3, 2015 as depicted

24

in Figure 4.2 and Figure 4.3. In general, the increase in stem density is the cause for the increase in the mean sigma nought values that produced the first peak. The sigma nought values then decrease as the leaf coverage the thin scatterers (the stems) increases. Then, the growth of flag leaves and young heads in the top layer of the crop canopy result in the increase in sigma nought values.
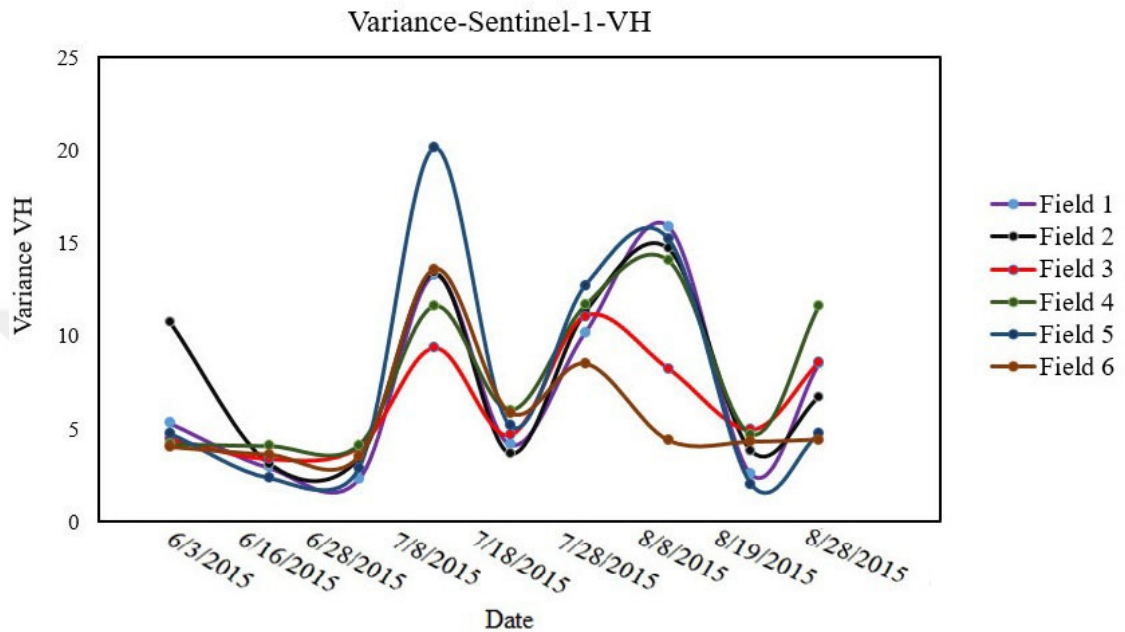

Figure 4.4 : The time series of variance of sigma nought (dB) in VH polarization in 2015.

For further analysis, the sigma nought values determined from the SAR satellite images captured on August 28, 2015 were selected as the data of field parameters measured using the CI-110 device were available only for this date.

The backscattering coefficients of the paddy rice in the 6 fields extracted from the various polarizations (HH and VV in TerraSAR-X and VH and VV in Sentinel-1) of the SAR images are shown in Figure 4.6. In general, the backscattering coefficients determined from the image of TerraSAR-X were found to be larger than the corresponding values determined from the image of Sentinel-1. This could be related to the fact that TerraSAR-X is located more close to the ground (when compared to Sentinel-1) with better resolution, high frequency and the more number of pixels. The TerraSAR-X image was captured on 4 September 2015 and the Sentinel-1 image was captured on 27 August 2015. It can be seen from this figure that, in all of the 6 rice fields, the largest backscattering coefficient values were determined from the SAR
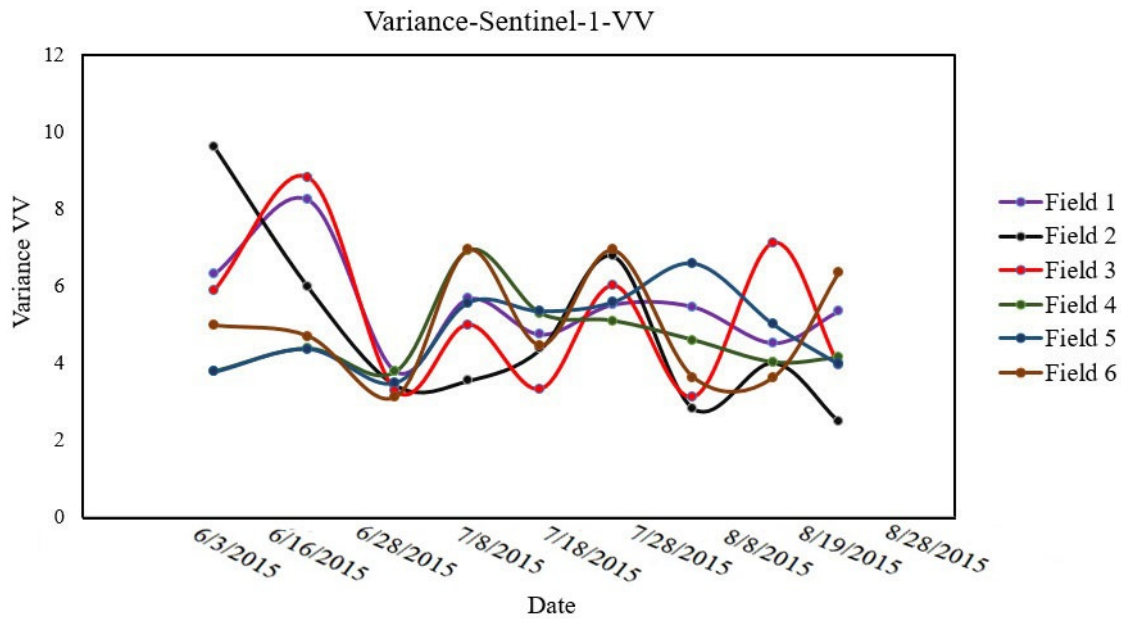
Figure 4.5 : The time series of variance of sigma nought (dB) in VV polarization in 2015.

image in HH polarization. As opposed this, the smallest backscattering coefficients of rice in the 6 fields were determined from the SAR images in cross polarization (VH). These values indicate that rice crop fields have the strongest response to the HH polarization while they have the weakest response to the cross polarization. It can also be seen from Figure 4.6 that the backscattering coefficients of the 6 fields in the VV polarizations of both SAR images is between the corresponding backscattering values in HH and VH polarizations of the TerraSAR-X and Sentinel-1 satellites, respectively. The backscattering coefficients determined under the HH polarization of TerraSAR-X image were found to be the highest in all of the rice fields. Based on these analyses, the HH polarization provides the best discrimination between water and non-water terrains. This is caused by the low scattering of the horizontal component of the signal from the smooth open water surface.

The scatter plots developed using the measured LAI values and backscattering coefficient values of the Sentinel-1 (with VH and VV polarizations) and TerraSAR-X (HH and VV polarizations) images are depicted in Figure 4.7.

As can seen from Figure 4.7, in general, the LAI values computed using the backscattering coefficients determined from the TerraSAR-X satellite in the HH polarization were found to be better correlated with the measured LAI values than
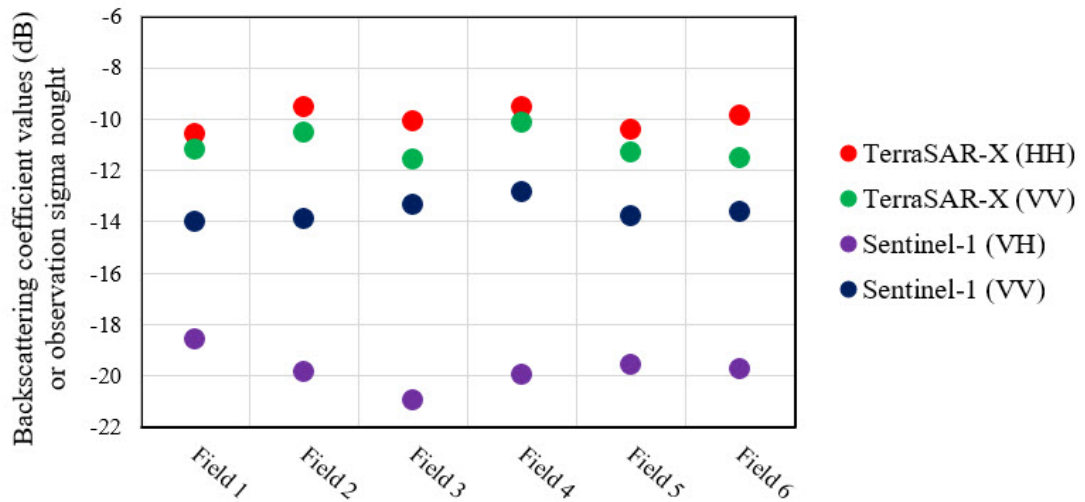
26

Figure 4.6 : The backscattering coefficients of rice in the 6 fields for TerraSAR-X (HH and VV) and Sentinel-1 (VH and VV)

the Sentinel-1 satellite. This could be attributed to the fact that, as also witnessed by [54], the EM sent from the sensor with HH polarization interacts more with the vertical structure of the paddy rice crop (leaf size and stem density oriented in the vertical direction) than the horizontal structure of the crop (leaf size and stem density oriented in the horizontal direction).

In addition, this could be related to that fact that TerraSAR-X is located close to the ground to (when compared to Sentinel-1) with better resolution and high frequency. However, the LAI value measured using backscattering coefficients determined using the TerraSAR-X image with HH polarization resulted in the largest values of correlation coefficients (0.778) or correlation determination (0.605) and the littlest values of correlation determination is for TerraSAR-X image with VV polarization with 0.292.

4.3 WCM analysis

Analysis based on the WCM use two different SAR frequencies. In this study, the possibility of extracting information about vegetation parameters A and B from Sentinel-1 (C-band at 5.35 GHZ frequency and 44.7 incidence angle) and TerraSAR-X (X-band at 9.65 GHZ frequency and 36.8 incidence angle) were investigated. Parameter A corresponds to the albedo of the vegetation and parameter B is an
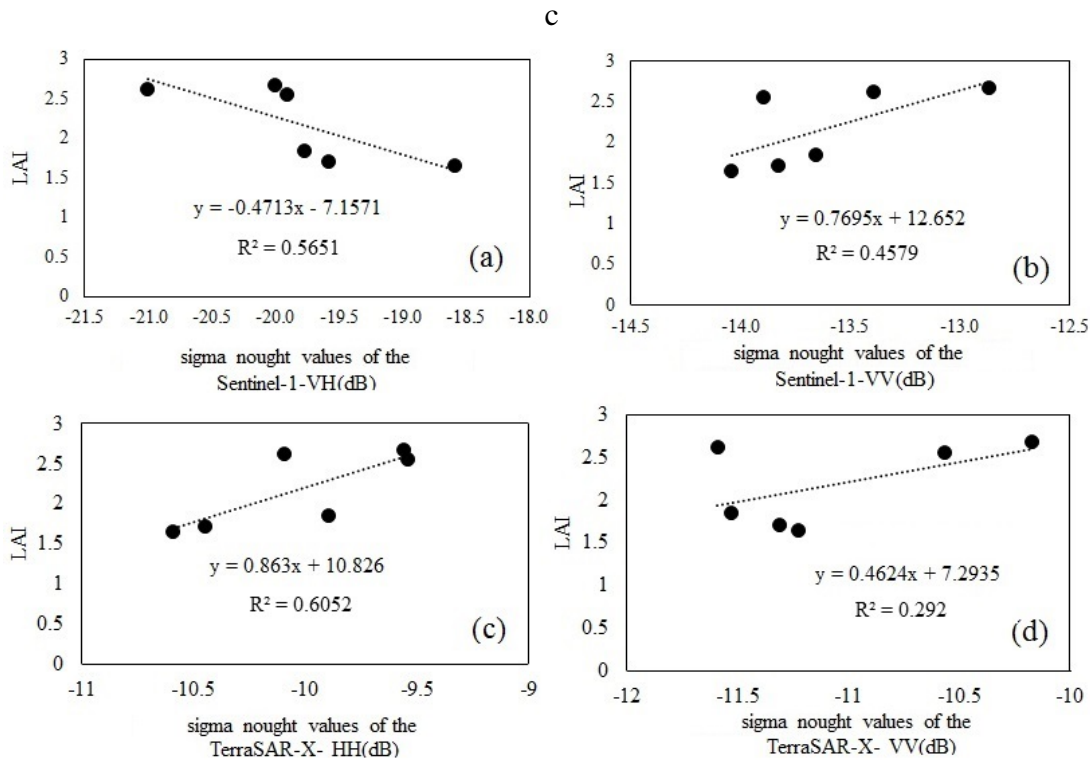
c

Figure 4.7 : The scatter plots of observation sigma nought values of the Sentinel-1 (a,b) and TerraSAR-X (c,d)

attenuation factor. Because of its larger wave length, the backscatter of C-band (with length of 6 cm) is expected to have stronger penetration in to the target than the backscatter of X-band (with length of 3 cm).

The values of the two parameters (parameters A and B that depend on the type of vegetation) estimated from the backscatter values of the HH and VV polarizations in TerraSAR-X and VH and VV polarizations in Sentinel-1 are presented in Table 4.2 (A GA optimization technique was coupled with the water cloud model for the estimation of the vegetation parameters A and B). The values of parameter B and the lower values of parameter A presented in the table show the presence of greater influence of vegetation on the recorded signal. Higher value of parameter B shows the presence of attenuation and contributes to a larger vegetation descriptor effect on sigma nought.

By taking in to consideration the values of the standard deviation of parameters of A and B presented in Table 4.2, it can be said that there are no variations in the values of parameter A determined from Sentinel-1 VV, TerraSAR-X VV and TerraSAR-X HH images when compared with the standard deviation values of the Sentinel-1 VH image, which was found to be relatively larger. The standard deviations of parameter

28

Table 4.2 : Parameter values obtained with GA with $N = 22$

Radar	A		B		RMSE [dB]
Acquisition	mean	std	mean	std	$\sigma^0_{obs} - \sigma^0_{comp}$
Sentinel-1 VV	-0.015	0.003	0.224	0.574	0.00009
Sentinel-1 VH	-0.005	0.001	0.489	0.233	0.00011
TerraSAR-X VV	-0.024	0.004	0.482	0.907	0.00015
TerraSAR-X HH	-0.028	0.005	1.235	0.731	0.01499

B estimated from the SAR images of all polarizations were found to be larger and, hence, there are larger variations in the values of Parameter B. The RMSE values presented in Table 4.2 show that the observed and computed sigma nought values are very close to each other. However, the RMSE value of TerraSAR-X HH was found to be slightly higher when compared to the other RMSE values presented in the table. This could be attributed to the presence of larger vegetation descriptor effect on the observed sigma nought. In addition, WCM based sigma nought values (computed sigma nought values) of the TerraSAR-X images were found to be not close to the observed sigma nought (determined with SNAP). As opposed to this, the observed and computed sigma nought values of the Sentinel-1 images were found to be very close to each other. This is because the Sentinel-1 sensor has a longer wavelength can be more sensitive to vegetation [55].

Among the six fields, three field were selected after checking all possible combinations of fields for calibration and validation. Then, A and B values of the three selected fields were determined by WCM from the measured LAI values of the three fields. These A and B values were then used as inputs (together with other required inputs) in WCM to determine the LAI of the remaining three fields.

The same steps were repeated twenty times to estimate values of LAI index from A and B values of various combinations of three fields. This means that, for instance, for the VH polarization of Sentinel-1, A and B values were determined from the mean values of characteristics of the image determined for the three selected fields as input into the WCM model. The computed A and B values were, then, used as inputs into the WCM model together with other required characteristics of the remaining three fields to determine LAI values for each of the three field. These procedure was repeated

by considering various combinations of fields for training and testing. A total of 20 combinations (scenarios) were developed using the six fields. Table 4.3 presents the combination of fields used for training and testing under each scenario.

Table 4.3 : Test and training scenario

Senario NO	Train	Test	Senario NO	Train	Test
1	Field 1-3-5	Field 2-4-6	11	Field 2-4-6	Field 1-3-5
2	Field 1-2-3	Field 4-5-6	12	Field 4-5-6	Field 1-2-3
3	Field 1-2-4	Field 3-5-6	13	Field 3-5-6	Field 1-2-4
4	Field 1-2-5	Field 3-4-6	14	Field 3-4-6	Field 1-2-5
5	Field 1-2-6	Field 3-4-5	15	Field 3-4-5	Field 1-2-6
6	Field 1-3-4	Field 2-5-6	16	Field 2-5-6	Field 1-3-4
7	Field 1-3-6	Field 2-4-5	17	Field 2-4-5	Field 1-3-6
8	Field 1-5-6	Field 2-3-4	18	Field 2-3-4	Field 1-5-6
9	Field 1-4-6	Field 2-3-5	19	Field 2-3-5	Field 1-4-6
10	Field 1-4-5	Field 2-3-6	20	Field 2-3-6	Field 1-4-5

The same steps were followed for the VV polarization of Sentinel-1 image and the HH and VV polarizations of the TerraSAR-X images. Then correlation values between the LAI values of each fields determined using the above mentioned procedure and the corresponding in-situ LAI values were determined. Figures 4.8, 4.9, 4.10 and 4.11 depict the correlation values determined between the simulated and *in-situ* LAI values of the 20 scenarios.

As can be seen from Figure 4.8, higher correlation coefficients (-0.999, -0.998 and -0.996) were found under scenarios 3, 13 and 7 for Sentinel-1 VH polarization respectively. The lowest correlation coefficient was found under scenario 8. By taking into consideration Figure 4.9, scenarios 2, 8, 20 and 19 were found to result in higher correlation coefficient values (0.999, 0.997, 0.995 and 0.992 respectively) for Sentinel-1 VV polarization. The lowest correlation coefficient was found under scenario 6. Scenarios 14, 20, 13 and 18 were found to result in higher correlation coefficient values in figure 4.10 (0.999, 0.998, 0.992 and 0.991 respectively) for TerraSAR-X, HH polarization. Smaller correlation coefficients were observed under scenarios 3, 4, 8 and 10. Finally, for TerraSAR-X VV polarization, scenarios 18, 20,

1 and 11 were found to result in higher correlation coefficient values (-0.999, 0.993, 0.988 and -0.986 respectively) (Figure 4.11).

Sentinel-1 (VH)

Figure 4.8 : The scatter plots of correlation coefficient under various scenarios for Sentinel-1 VH polarization
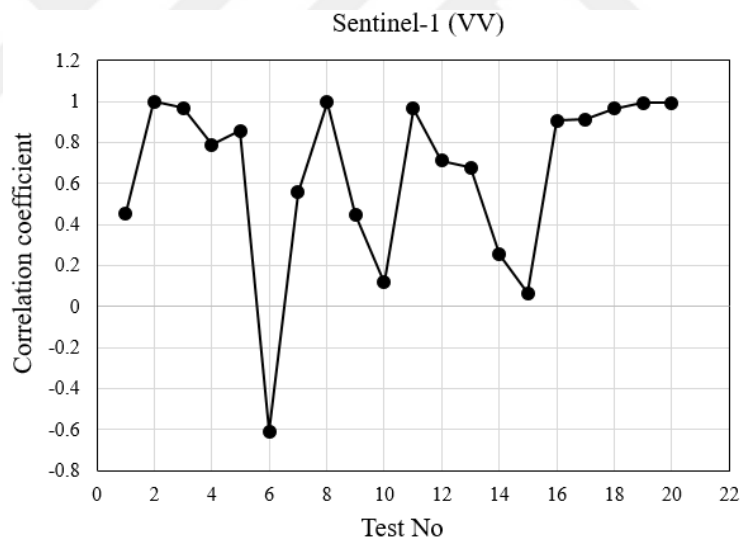
Sentinel-1 (VV)

Figure 4.9 : The scatter plots of correlation coefficient under various scenarios for Sentinel-1 VV polarization

Root Mean Square Error (RMSE) and Normalized Relative Mean Error (RME) values were used as evaluation criteria to assess the performance of the WCM in estimating LAI values from the various polarizations of the SAR images. RMSE measures the difference between the estimated (using WCM) and *in-situ* values of LAI, whereas RME measures the relative difference between the estimated and *in-situ* values of LAI. Equations 4.1 and 4.2 are used to determine these evaluation criteria. As both RMSE and RME are functions of the differences between estimated and *in-situ* values, the
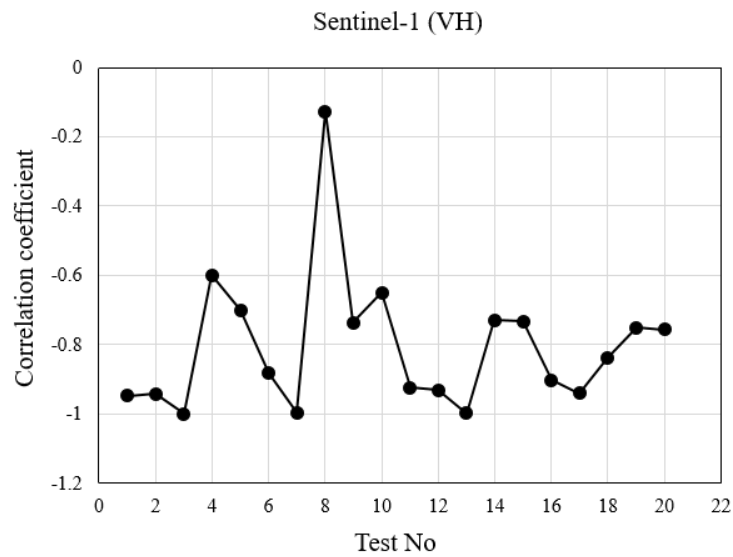
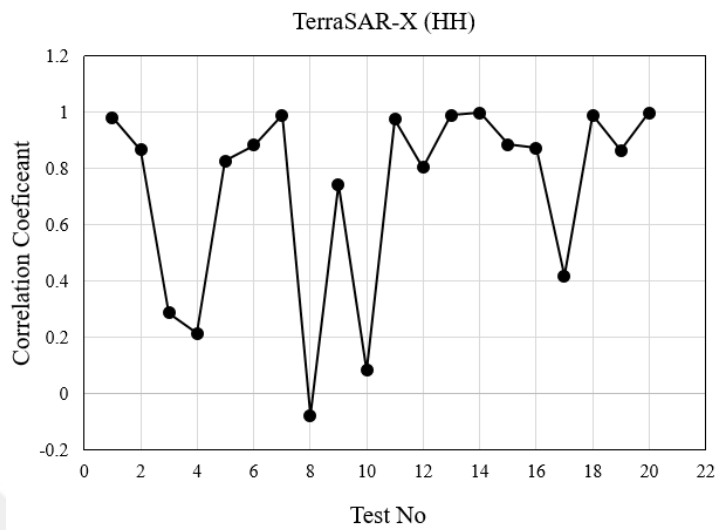**Figure 4.10** : The scatter plots of correlation coefficient under various scenarios for TerraSAR-X HH polarization
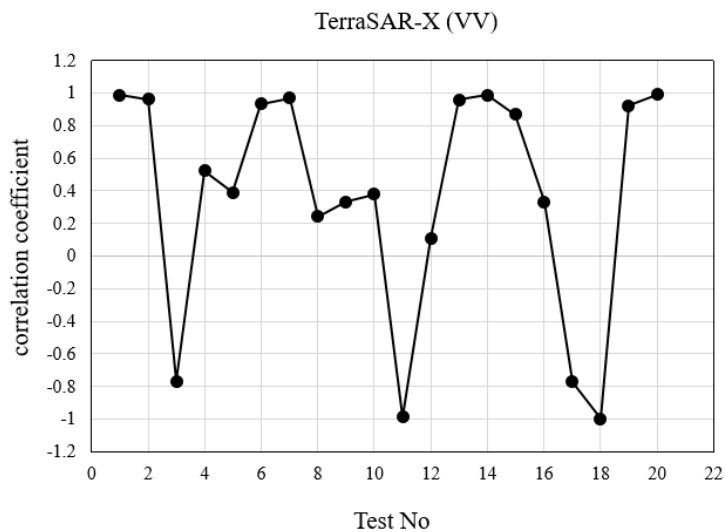

Figure 4.11 : The scatter plots of correlation coefficient under various scenarios for TerraSAR-X VV polarization

smaller the values of these indices (close to zero) the higher the performance of the model.

$$RMSE = \sqrt{1/N \sum_{i=1}^{N} (h_{measured} - h_{estimated})^2} \qquad (4.1)$$

$$RME = (h_{estimated} - h_{measured})/h_{measured} \qquad (4.2)$$

The RMSE values of the various polarizations of the two SAR images is determine with Equations 4.1. The RSME of VH and VV polarization of Sentinel-1 are 0.69 and 0.47, respectively. The result for in general, the RMSE values determined under the VV polarization of Sentinel-1 were found to be smaller than the corresponding values determined under VH polarization. In addition to the RSME of VH and VV polarization of TerraSAR-X are 0.457 and 0.467 respectively. The result for in general, the RMSE values determined under the HH polarization of TerraSAR-X were found to be smaller than the corresponding values determined under VV polarization.

The RME values of the various polarizations of the two SAR images are given in Table 4.4. The RME values in this table show that, the largest value was found for field 1 under both polarizations, where as the smallest value of RME was found for field 2 under the VH polarization and field 4 under the VV polarization. Nevertheless, as presented in Table 4.4, the RME values under the VV polarization are smaller than the RME values under the VH polarization. These show that the Sentinel-1 image with VV polarization is better for LAI estimation than the Sentinel-1 image with VH.

Table 4.4 : Results of the performance evaluation criteria for TerraSAR-X and Sentinel-1

	RME			
	Sentinel-1 (VH)	Sentinel-1 (VV)	TerraSAR-X (HH)	TerraSAR-X (VV)
Field 1	0.604	0.315	0.293	0.352
Field 2	-0.184	-0.204	-0.128	-0.120
Field 3	-0.309	-0.183	-0.211	-0.253
Field 4	-0.241	-0.152	-0.182	-0.138
Field 5	0.363	0.290	0.258	0.280
Field 6	0.218	0.204	0.229	0.146

4.4 Vegetation index analysis

In order to establish a relationship between LAI values and the ZWSI, SR, GMI and GNDVI indices of the paddy rice crop, the values of these indices were determined from the satellite image of the study area captured on August 28, 2015 using Landsat-8. The mean values of these indices are presented in Table 4.5. It can be seen from this table that the maximum values of the NDWI (-0.785), NDVI (0.770), GNDVI (0.712) and SR (8.741) indices were found in field-3. In addition, the maximum values of the ZWSI (2.239) indices were found in field-4, whereas the maximum value of the GMI index (1.203) was found in field-1. Correlation analysis was then undertaken to investigate the relationship between the values of these indices and the field measured LAI values.

Table 4.5 : Mean values of vegetation indices for the fields determined from Landsat-8.

Field No	NDWI	NDVI	GNDVI	GMI	SR	ZWSI
Field 1	-0.654	0.654	0.628	1.203	4.882	2.0712
Field 2	-0.753	0.756	0.692	1.038	7.357	2.064
Field 3	-0.785	0.770	0.712	1.160	8.741	2.237
Field 4	-0.753	0.761	0.704	1.126	7.828	2.239
Field 5	-0.711	0.712	0.670	1.138	6.259	2.118
Field 6	-0.686	0.667	0.638	0.998	5.399	1.725

In *in-situ* LAI measurements are tightly correlated with spectral are indices as summarized in Figure 4.12. Figure 4.12 (a, b, c and d) depicts the scatter plot developed using the measured LAI values and the values of the SR, NDVI, NDWI, and GNDVI indices with a linear fit line and the corresponding values of the coefficient of determination. It can be seen from this figure that the SR index was found to be best correlated with the measured LAI value (with coefficient of determination value of 0.832), followed by the NDVI, NDWI and GNDVI indices (with coefficient of determination value of 0.831, 0.820 and 0.807 respectively).

It can be seen from the correlation coefficient values presented in Table 4.6 that, in general, the relationship between the GMI index and the other indices is weaker than the relationship among the other indices, followed by the relationship between the ZWSI index and the other indices. The correlation coefficient between NDVI and
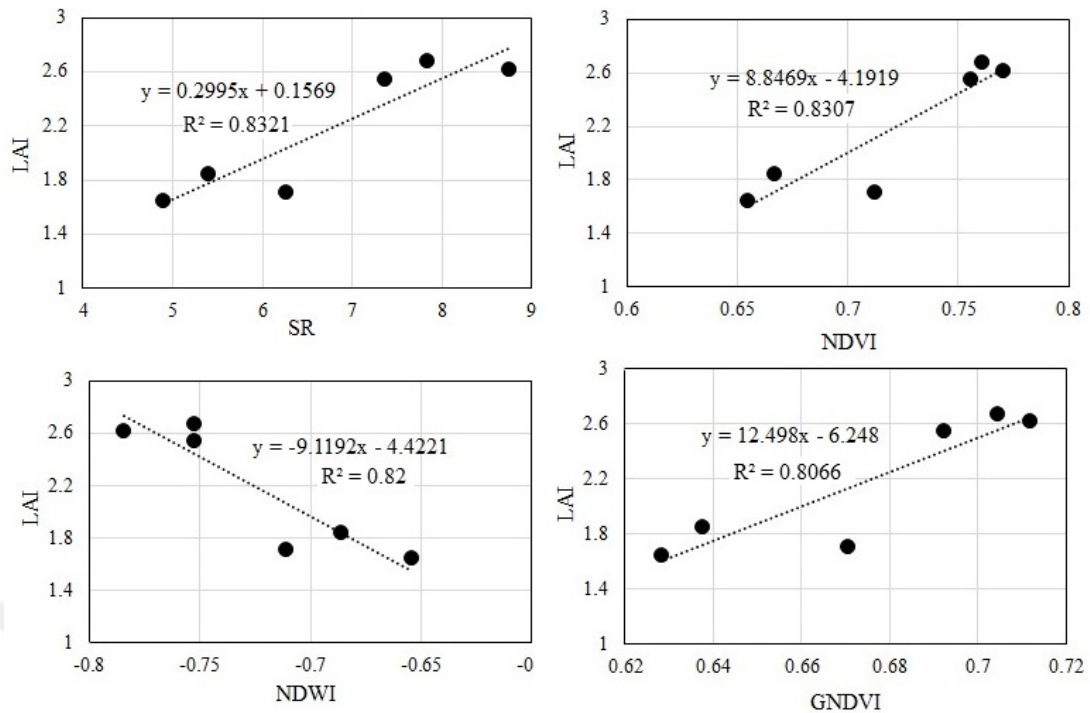
Figure 4.12 : The scatter plots of indices

GNDVI is largest positive value (0.995), whereas the one between GMI and NDVI is the smallest positive value (0.012). In terms of negative relationships, the values in Table 4.6 show that there exists a strong negative correlation between SR and NDWI indices (-0.989), while there exists a weak negative relationship between LAI and GMI indices (-0.117). By taking into consideration the correlation coefficient values between the indices and the *in-situ* LAI values, the comparison of the GMI correlation shows that many of the analysed vegetation indices in this study provide quite high correlation coefficient. Thus, it is possible to conclude that the vegetation indices considered in this study are much more sensible to the paddy rice field than the GMI, with the exception ZWSI, where there exists moderate relationship. It is also worth to notice that the vegetation indices that correlated better to each other (like the relationship among NDVI, NDWI, GNDVI and SR) were found to be better correlated to the *in-situ* LAI values. Therefore, it is possible to conclude that these indices are the best.

4.5 Correlation analysis within remote-sensing images

As a means of inter-comparing the performance of the SAR image based and Landsat-8 based LAI estimation, a bar graph was used. Figure 4.13 depicts the bar graph

Table 4.6 : Mean values of vegetation indices for the fields determined from Landsat-8.

	NDWI	NDVI	GNDVI	GMI	SR	ZWSI	LAI
NDWI	1	-0.976	-0.978	0.065	-0.989	-0.592	-0.906
NDVI	-0.976	1	0.995	0.012	0.973	0.695	0.911
GNDVI	-0.978	0.995	1	0.058	0.983	0.717	0.898
GMI	0.065	0.012	0.058	1	0.065	0.708	-0.117
SR	-0.989	0.973	0.983	0.065	1	0.679	0.912
ZWSI	-0.592	0.695	0.717	0.708	0.679	1	0.536
LAI	-0.906	0.911	0.898	-0.117	0.912	0.536	1

developed based on the values of the correlation coefficients of the ground-based and remote sensing based LAI estimations. The figure also depicts the correlation values determined between the *in-situ* LAI and the various field measured biophysical parameters.
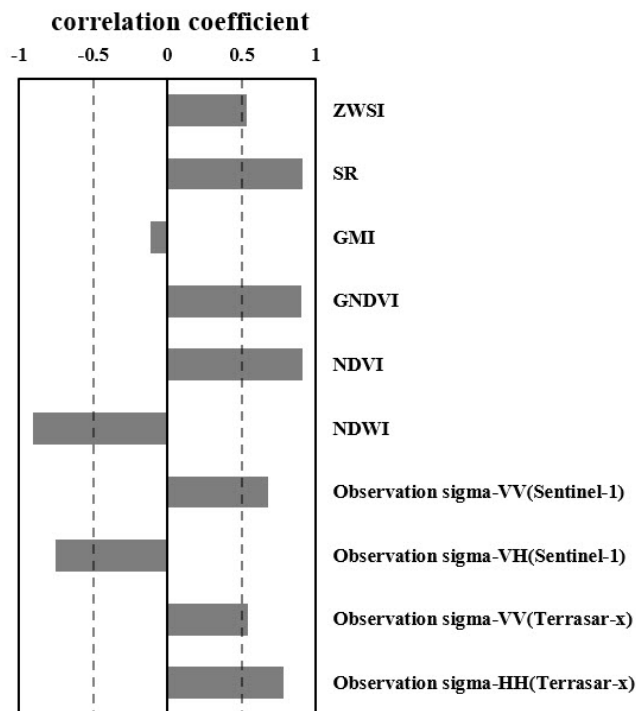

Figure 4.13 : The values of the correlation coefficients of the ground-based and remote sensing based LAI estimations

It can be clearly seen from this figure that the SR, NDVI, NDWI and GNDVI indices of the Landsat-8 image were found to be much better correlated to the *in-situ* LAI values better than the LAI values estimated from the backscattering coefficients of the

TerraSAR-X image with HH polarization. Therefore, it can be stated, from the above given inter-comparison, that optical sensor (Landsat-8) images are better sources of data for the quick and accurate estimation of the LAI value of the paddy rice crop in the study area than SAR (Sentinel-1 and TerraSAR-X) images.

The number of pixels that cover each field of the paddy rice under the two SAR images and the Landsat-8 image are presented in Table 4.7. As can be seen from the table, the number of pixels of the fields of Landsat-8 image range from 18 (field 1) to 36 (field 3). By taking into consideration the number of pixels from the Sentinel-1 image, the number ranges from 130 (field 1) to 297 (field 3).

Table 4.7 : Samples of 6 fields for TerraSAR-X, Sentinel-1 and Landsat-8

	# Samples		
	TerraSAR-X	Sentinel-1	Landsat-8
Field 1	406	130	18
Field 2	722	193	25
Field 3	536	297	36
Field 4	280	282	33
Field 5	379	288	34
Field 6	500	276	32

Table 4.8 is given to present the cross correlation values determined between the polarization that best simulated LAI (HH for TerraSAR-X and VH for Sentinel-1) and the SR index of the Landsat-8 image that was found to be best correlated to LAI. As can be seen from the table, the largest cross-correlation value (-0.880) was found to be between the VH polarization of Sentinel-1 and the SR index of Landsat-8 images. The negative sign shows the presence of inverse relationship.

Table 4.8 : Cross correlation values of the two SAR images

	TerraSAR-X	Sentinel-1	Landsat-8
TerraSAR-X	1	-0.488	0.532
Sentinel-1	-0.488	1	-0.880
Landsat-8	0.532	-0.880	1

5. CONCLUSIONS AND RECOMMENDATIONS

Acquiring reliable and accurate LAI values rapidly is an essential to study ecosystem processes and undertake process-based ecological research. For large spatial extents, however, is difficult to directly acquire LAI because of its time consuming and work intensive nature. In this study, the satellite images were used as data sources to compute rapidly and accurately LAI values of paddy rice crop at reproductive stage, which is the most heterogeneous period of the growth cycle of the crop. This study analyzed the presence of relations between *in-situ* measures LAI and backscattering coefficients determined from SAR images having various polarizations, and vegetation indices computed from optical image (image from Landsat-8). The following conclusions can be drawn from the results of the study:

• The correlations obtained between the in-situ LAI and the values of the field parameters were not found to be good except with the Transmission Coefficient, which was found to be about -0.9048.

• The correlations between the in-situ LAI and the backscattering coefficients computed from the SAR images with various polarizations were found to be weak with the R^2 values of the Sentinel-1 VH, Sentinel-1 VV, TerraSAR-X HH and TerraSAR-X VV polarizations being about 0.57, 0.46, 0.61 and 0.29, respectively.

• The correlations obtained between the *in-situ* LAI and the vegetation indices generated from the Landsat-8 image were, in general very good except with the ZWSI (0.29) and GMI (0.01) indices.

• In particular, the correlations obtained between the *in-situ* LAI and the SR, NDVI, NDWI and GNDVI indices were found to be very good with the R^2 values of the 0.832, 0.830, 0.820 and 0.810, respectively, that SR with 0.832 being the highest.

• The indices given as functions of NIR EM radiation resulted in higher correlation.

• From the performances of the SR and NDVI indices, it could be understood that normalization can slightly decrease the correlation coefficient values.

Therefore, the LAI at the reproductive stage of paddy rice crops at a large scale can be mapped using simple linear relationships with the SR, NDVI, NDWI and GNDVI indices. However, since this study was based on only one variety of rice and in one particular area, undertaking a similar research in various geographical regions by considering various rice species and different growth stages would be an interesting research topic for the future.

REFERENCES

[1] **Hegde, S. and Hegde, V.** (2013). Assessment of global rice production and export opportunity for economic development in Ethiopia, *Int. J. Sci. Res*, *2*, 257–260.

[2] **Faure, J. and Mazaud, F.** (1994). [Rice quality criteria and the European market], *Comision Internacional del Arroz. Reunion. 18, Rome (Italy), 5-9 Sep 1994*.

[3] **Wijesingha, J., Deshapriya, N. and Samarakoon, L.** (2015). Rice Crop Monitoring and Yield Assessment with MODIS 250m Gridded Vegetation Products: A Case Study of Sa Kaeo Province, Thailand, *The International Archives of Photogrammetry, Remote Sensing and Spatial Information Sciences*, *40*(7), 121.

[4] **Watson, D.J.** (1947). Comparative physiological studies on the growth of field crops: I. Variation in net assimilation rate and leaf area between species and varieties, and within and between years, *Annals of Botany*, *11*(41), 41–76.

[5] **Motohka, T., Nasahara, K., Miyata, A., Mano, M. and Tsuchida, S.** (2009). Evaluation of optical satellite remote sensing for rice paddy phenology in monsoon Asia using a continuous in situ dataset, *International Journal of Remote Sensing*, *30*(17), 4343–4357.

[6] **Zarate-Valdez, J.L., Whiting, M.L., Lampinen, B.D., Metcalf, S., Ustin, S.L. and Brown, P.H.** (2012). Prediction of leaf area index in almonds by vegetation indexes, *Computers and electronics in agriculture*, *85*, 24–32.

[7] **Zheng, G., Moskal, L.M. and Kim, S.H.** (2013). Retrieval of effective leaf area index in heterogeneous forests with terrestrial laser scanning, *IEEE Transactions on Geoscience and Remote Sensing*, *51*(2), 777–786.

[8] **Majasalmi, T., Rautiainen, M., Stenberg, P. and Rita, H.** (2012). Optimizing the sampling scheme for LAI-2000 measurements in a boreal forest, *Agricultural and forest meteorology*, *154*, 38–43.

[9] **Yan, G., Hu, R., Wang, Y., Ren, H., Song, W., Qi, J. and Chen, L.** (2016). Scale Effect in Indirect Measurement of Leaf Area Index, *IEEE Transactions on Geoscience and Remote Sensing*, *54*(6), 3475–3484.

[10] **Bréda, N.J.** (2003). Ground-based measurements of leaf area index: a review of methods, instruments and current controversies, *Journal of experimental botany*, *54*(392), 2403–2417.

[11] **Jonckheere, I.**, **Fleck, S.**, **Nackaerts, K.**, **Muys, B.**, **Coppin, P.**, **Weiss, M. and Baret, F.** (2004). Review of methods for in situ leaf area index determination: Part I. Theories, sensors and hemispherical photography, *Agricultural and forest meteorology*, *121*(1), 19–35.

[12] **Brandão, Z.N. and Zonta, J.H.** (2016). Hemispherical photography to estimate biophysical variables of cotton, *Revista Brasileira de Engenharia Agrícola e Ambiental*, *20*(9), 789–794.

[13] **Baghdadi, N.N.**, **El Hajj, M.**, **Zribi, M. and Fayad, I.** (2016). Coupling SAR C-band and optical data for soil moisture and leaf area index retrieval over irrigated grasslands, *IEEE Journal of Selected Topics in Applied Earth Observations and Remote Sensing*, *9*(3), 1229–1243.

[14] **Inoue, Y.**, **Sakaiya, E. and Wang, C.** (2014). Capability of C-band backscattering coefficients from high-resolution satellite SAR sensors to assess biophysical variables in paddy rice, *Remote Sensing of Environment*, *140*, 257–266.

[15] **Huang, H. and Lian, J.** (2015). A 3D approach to reconstruct continuous optical images using lidar and MODIS, *Forest Ecosystems*, *2*(1), 1.

[16] **Yebra, M. and Chuvieco, E.** (2009). Linking ecological information and radiative transfer models to estimate fuel moisture content in the Mediterranean region of Spain: Solving the ill-posed inverse problem, *Remote Sensing of Environment*, *113*(11), 2403–2411.

[17] **Privette, J.L.** (1994). An efficient strategy for the inversion of bidirectional reflectance models with satellite remote sensing data, *Ph.D. thesis*, University of Colorado.

[18] **Ozdogan, M.**, **Yang, Y.**, **Allez, G. and Cervantes, C.** (2010). Remote sensing of irrigated agriculture: Opportunities and challenges, *Remote sensing*, *2*(9), 2274–2304.

[19] **Gao, S.**, **Niu, Z.**, **Huang, N. and Hou, X.** (2013). Estimating the Leaf Area Index, height and biomass of maize using HJ-1 and RADARSAT-2, *International Journal of Applied Earth Observation and Geoinformation*, *24*, 1–8.

[20] **Zhang, Y.**, **Liu, X.**, **Su, S. and Wang, C.** (2014). Retrieving canopy height and density of paddy rice from Radarsat-2 images with a canopy scattering model, *International Journal of Applied Earth Observation and Geoinformation*, *28*, 170–180.

[21] **Campos-Taberner, M.**, **García-Haro, F.J.**, **Camps-Valls, G.**, **Grau-Muedra, G.**, **Nutini, F.**, **Crema, A. and Boschetti, M.** (2016). Multitemporal and multiresolution leaf area index retrieval for operational local rice crop monitoring, *Remote Sensing of Environment*, *187*, 102–118.

[22] **Dong, J.**, **Xiao, X.**, **Menarguez, M.A.**, **Zhang, G.**, **Qin, Y.**, **Thau, D.**, **Biradar, C. and Moore, B.** (2016). Mapping paddy rice planting area in northeastern Asia with Landsat 8 images, phenology-based algorithm and Google Earth Engine, *Remote Sensing of Environment*.

[23] **DeFries, R., Achard, F., Brown, S., Herold, M., Murdiyarso, D., Schlamadinger, B. and de Souza, C.** (2007). Earth observations for estimating greenhouse gas emissions from deforestation in developing countries, *Environmental science & policy*, *10*(4), 385–394.

[24] **Aggarwal, S.** (2004). Principles of remote sensing, *Satellite remote sensing and GIS applications in agricultural meteorology*, *23*.

[25] **Center, N.S.** (2011). Assessment of research areas with great EO support potential, *Ph.D. thesis*, Alfred Wegener Institute for Polar and Marine Research, Germany.

[26] **Clevers, J. and Van Leeuwen, H.** (1996). Combined use of optical and microwave remote sensing data for crop growth monitoring, *Remote Sensing of Environment*, *56*(1), 42–51.

[27] **Kuenzer, C. and Knauer, K.** (2013). Remote sensing of rice crop areas, *International Journal of Remote Sensing*, *34*(6), 2101–2139.

[28] **Attema, E. and Ulaby, F.T.** (1978). Vegetation modeled as a water cloud, *Radio science*, *13*(2), 357–364.

[29] **Alajmi, A. and Wright, J.** (2014). Selecting the most efficient genetic algorithm sets in solving unconstrained building optimization problem, *International Journal of Sustainable Built Environment*, *3*(1), 18–26.

[30] **Rees, W.G.** (2005). *Remote sensing of snow and ice*, CRC press.

[31] **Anthony, E.** (2012). Shortcomings Common to Real Remote Sensing Systems.

[32] **Zheng, G. and Moskal, L.M.** (2009). Retrieving leaf area index (LAI) using remote sensing: Theories, methods and sensors, *Sensors*, *9*(4), 2719–2745.

[33] **Viña, A., Gitelson, A.A., Nguy-Robertson, A.L. and Peng, Y.** (2011). Comparison of different vegetation indices for the remote assessment of green leaf area index of crops, *Remote Sensing of Environment*, *115*(12), 3468–3478.

[34] **Hall, A., Lamb, D., Holzapfel, B. and Louis, J.** (2002). Optical remote sensing applications in viticulture-a review, *Australian Journal of Grape and Wine Research*, *8*(1), 36–47.

[35] **Lee, K.S., Cohen, W.B., Kennedy, R.E., Maiersperger, T.K. and Gower, S.T.** (2004). Hyperspectral versus multispectral data for estimating leaf area index in four different biomes, *Remote Sensing of Environment*, *91*(3), 508–520.

[36] **Rouse Jr, J., Haas, R., Schell, J. and Deering, D.** (1974). Monitoring vegetation systems in the Great Plains with ERTS, *NASA special publication*, *351*, 309.

[37] **Lillesand, T., Kiefer, R.W. and Chipman, J.** (2014). *Remote sensing and image interpretation*, John Wiley & Sons.

[38] **Jordan, C.F.** (1969). Derivation of leaf-area index from quality of light on the forest floor, *Ecology*, *50*(4), 663–666.

[39] **Gitelson, A.A.**, **Kaufman, Y.J. and Merzlyak, M.N.** (1996). Use of a green channel in remote sensing of global vegetation from EOS-MODIS, *Remote Sensing of Environment*, *58*(3), 289–298.

[40] **Gitelson, A.A. and Merzlyak, M.N.** (1997). Remote estimation of chlorophyll content in higher plant leaves, *International Journal of Remote Sensing*, *18*(12), 2691–2697.

[41] **Zygielbaum, A.I.**, **Gitelson, A.A.**, **Arkebauer, T.J. and Rundquist, D.C.** (2009). Non-destructive detection of water stress and estimation of relative water content in maize, *Geophysical Research Letters*, *36*(12).

[42] **Prevot, L.**, **Champion, I. and Guyot, G.** (1993). Estimating surface soil moisture and leaf area index of a wheat canopy using a dual-frequency (C and X bands) scatterometer, *Remote Sensing of Environment*, *46*(3), 331–339.

[43] **Inoue, Y.**, **Kurosu, T.**, **Maeno, H.**, **Uratsuka, S.**, **Kozu, T.**, **Dabrowska-Zielinska, K. and Qi, J.** (2002). Season-long daily measurements of multifrequency (Ka, Ku, X, C, and L) and full-polarization backscatter signatures over paddy rice field and their relationship with biological variables, *Remote Sensing of Environment*, *81*(2), 194–204.

[44] **Erten, E.**, **Rossi, C. and Yuzugullu, O.** (2015). Polarization impact in TanDEM-X data over vertical-oriented vegetation: the paddy-rice case study, *Geoscience and Remote Sensing Letters, IEEE*, *12*(7), 1501–1505.

[45] **Yuzugullu, O.**, **Erten, E. and Hajnsek, I.** (2017). Estimation of rice crop height from X-and C-band PolSAR by metamodel-based optimization, *IEEE Journal of Selected Topics in Applied Earth Observations and Remote Sensing*, *10*(1), 194–204.

[46] **Attema, E.**, **Bargellini, P.**, **Edwards, P.**, **Levrini, G.**, **Lokas, S.**, **Moeller, L.**, **Rosich-Tell, B.**, **Secchi, P.**, **Torres, R.**, **Davidson, M.** *et al.* (2007). Sentinel-1-the radar mission for GMES operational land and sea services, *ESA bulletin*, *131*, 10–17.

[47] **Velotto, D.**, **Bentes, C.**, **Tings, B. and Lehner, S.** First Comparison of Sentinel-1 and TerraSAR-X data in the framework of maritime targets detection: South Italy case.

[48] **Snoeij, P.**, **Attema, E.**, **Davidson, M.**, **Floury, N.**, **Levrini, G.**, **Rosich, B. and Rommen, B.** (2008). Sentinel-1, the GMES radar mission, *2008 IEEE Radar Conference*, IEEE, pp.1–5.

[49] **Werninghaus, R.** (2004). TerraSAR-X mission, *Remote Sensing*, International Society for Optics and Photonics, pp.9–16.

[50] **Malhotra, R.**, **Singh, N. and Singh, Y.** (2011). Genetic algorithms: Concepts, design for optimization of process controllers, *Computer and Information Science*, *4*(2), 39.

[51] **Goldberg, D.** 1989, Genetic Algorithms in Search, Optimization, and Machine Learning, Addison-Wesley, Reading, MA.

[52] **McKinney, D.C. and Lin, M.D.** (1994). Genetic algorithm solution of groundwater management models, *Water Resources Research*, *30*(6), 1897–1906.

[53] **Goldberg, D.** Genetic algorithms in search, optimization, and machine learning, addison-wesley, reading, ma, 1989, *K. Ohno, K. Esfarjani, and Y Kawazoe: Computational Materi*.

[54] **Brisco, B.** (1998). Agricultural applications with radar, *Principles and applications in imaging radar*, 381–406.

[55] **Ali, I.**, **Cawkwell, F.**, **Dwyer, E.**, **Barrett, B. and Green, S.** (2016). Satellite remote sensing of grasslands: from observation to management—a review, *Journal of Plant Ecology*, rtw005.

CURRICULUM VITAE

Name Surname: Elnaz Najatishendi

Place and Date of Birth: 02.05.1987 Shendabad East Azerbaycan-IRAN

E-Mail: nejati.elnaz@gmail.com

EDUCATION:

- **B.Sc.:** Graduation year:2009, Computer Engineering, Islamic Azad University of Shabestar, East Azerbaycan-IRAN

- **M.Sc.:** Satellite Communication and Remote Sensing, Istanbul Technical University, Istanbul, TURKEY

PROFESSIONAL EXPERIENCE AND REWARDS:

09/2015-09/2016 - Research Assistant in TUBITAK Project ID: 113Y446